Deletion of the Envelope gene attenuates SARS-CoV-2 infection by altered Spike localization and increased cell-to-cell transmission

Hannah L. Fischer[1,2], Christopher Kline[1], W. Paul Duprex[1,2], Kevin R. McCarthy[1,2], Simon C. Watkins[3], James F. Conway[4], and Zandrea Ambrose[1,2]*

[1] Department of Microbiology and Molecular Genetics, University of Pittsburgh School of Medicine, Pittsburgh, PA
[2] Center for Vaccine Research, University of Pittsburgh, Pittsburgh, PA
[3] Department of Cell Biology, University of Pittsburgh School of Medicine, Pittsburgh, PA
[4] Department of Structural Biology, University of Pittsburgh School of Medicine, Pittsburgh, PA

* corresponding author: zaa4@pitt.edu

Abstract

Severe acute respiratory syndrome coronavirus 2 (SARS-CoV-2) causes COVID-19, a highly transmissible acute respiratory infection that can result in severe pneumonia and death. Many details of SARS-CoV-2 infection are not fully understood, including the cell biology and host-virus interactions involved in coronavirus assembly and release, in which the Envelope (E) structural protein is instrumental. Deletion of E in other coronaviruses has been shown previously to either attenuate or abrogate infection. To determine the role of E on SARS-CoV-2 virus production and infectivity, we produced reporter SARS-CoV-2 with or without the E gene deleted using a bacterial artificial chromosome. Replication of ΔE SARS-CoV-2 was attenuated in Vero E6 cells expressing human ACE2 and TMPRSS2 and in human epithelial cell lines. Electron and immunofluorescence microscopy and virology assays showed that ΔE SARS-CoV-2 increased cell surface expression of Spike (S) glycoprotein, leading to reduced S incorporation into ΔE SARS-CoV-2 particles and promotion of increased cell-to-cell transmission that evades neutralizing antibody inhibition. Trans-complementation of E partially rescued ΔE SARS-CoV-2 S incorporation and restored cell-free transmission. In addition to validating the role of E in retention of S in the ER-Golgi intermediate complex (ERGIC), our results showed that a lack of E led to reorganization of the ERGIC during SARS-CoV-2 infection. Improved understanding of E in SARS-CoV-2 replication and host pathogenesis may help development of novel therapeutics.

Importance

Non-S coronavirus structural proteins, including E, are conserved, making them potential pan-coronavirus therapeutic targets. Many details about these proteins and their roles in viral replication and host pathogenesis are unknown. In this study, we showed that SARS-CoV-2 replicates without E but is attenuated and impaired for virus particle formation, with less S incorporated into virions and more S expressed on the cell surface compared to wild-type virus. SARS-CoV-2 lacking E spread primarily via cell fusion and evaded neutralizing antibodies. In addition, the absence of E resulted in the reorganization of the ERGIC cell secretory compartment during SARS-CoV-2 infection. A better understanding of how E influences SARS-CoV-2 replication could guide directed design of novel therapeutics for treatment of COVID-19 patients, as well as the potential for pan-coronavirus protection against future coronavirus outbreaks.

Introduction

Severe acute respiratory syndrome coronavirus type 2 (SARS-CoV-2) is the third deadly coronavirus (CoV) to emerge in humans from zoonotic sources (1), preceded by SARS-CoV in 2002 (2) and Middle Eastern respiratory syndrome coronavirus (MERS-CoV) in 2012 (3). Infection with SARS-CoV-2 causes COVID-19, an acute respiratory infection that presents with mild to moderate symptoms in most individuals, which can result in severe pneumonia, multisystem inflammatory syndrome, multiple organ failure, and death (4–9). Since the start of the global pandemic in late 2019, there have been over 777 million cases of COVID-19 and over 7 million deaths reported worldwide as of January 2025 (10, 11). Post-acute sequelae are prominent with COVID-19, with over 10% of infected individuals developing Long COVID, consisting of over 200 identified symptoms, including long-term metabolic, cardiovascular, and neurological morbidities (12, 13).

Achievements in preventing and treating COVID-19 were rapidly developed to combat the pandemic. SARS-CoV-2 vaccines have been successful in preventing COVID-19, though protection conferred by either vaccines or natural infection lack long-term durability (14, 15). This is confounded by the rapid development of SARS-CoV-2 variants that evade immunity, requiring development and administration of vaccine boosters that target circulating variants, similar to seasonal influenza viruses (16–18). Most current treatments for COVID-19 in the U.S. are high-titer convalescent plasma or nonspecific small molecule antivirals that consist of repurposed inhibitors targeting viral enzymes common across multiple RNA viruses (19). Improved SARS-CoV-2 therapeutics are needed for higher specificity and efficacy, ideally against conserved CoV proteins that may offer pan-coronaviral protection.

SARS-CoV-2 is a β-coronavirus that is primarily transmitted via respiratory droplets and aerosols (20, 21) , infecting cells expressing the ACE2 receptor, most commonly epithelial cells within the upper airways and the gastrointestinal tract (22–25). The viral Spike (S) glycoprotein binds to ACE2 and is primed by the host protease furin and

subsequently activated for fusion and entry primarily by the host protease TMPRSS2 or, alternatively, Cathepsin B/L (26–28). Cytoplasmic release of the 30 kb single-stranded, positive-sense RNA viral genome results in ribosomal translation of the ORF1a/b open reading frame into the pp1a and pp1ab polyproteins, which are cleaved by two virally encoded proteases into the 16 nonstructural proteins (Nsps) comprising the viral replicase machinery (29, 30). Interaction of Nsps with host factors results in the formation of double membrane vesicles, in which the viral genome is both replicated and used as a template for discontinuous transcription of nested, co-terminal subgenomic RNAs (sgRNAs) that are translated into the viral structural and accessory proteins (29, 30). The membrane-bound S, Envelope (E), and Membrane (M) structural proteins along with the Nucleocapsid (N)-coated viral RNA genome are assembled into nascent virions within the endoplasmic reticulum/Golgi intermediate compartment (ERGIC) and released from the cell via vesicles (29, 30).

E is the smallest structural protein with only 75 amino acids, consisting of a short, luminal N-terminal domain (NTD); a transmembrane domain (TMD) that forms a calcium-selective channel in the lipid bilayer of the ERGIC membrane; and a cytosolic C-terminal domain (CTD) containing a PDZ-binding motif (PBM) that enables interaction with PDZ-containing host proteins (31–34). Expression of recombinant SARS-CoV E by transfection or during infection of cells results in colocalization with ERGIC proteins and it is not found in the ER or at the plasma membrane (35). E is conserved across CoVs and has three demonstrated roles in CoV replication: virus assembly, virus release, and host pathogenesis (36–40). However, the details for these roles are not completely understood.

While important for nascent virus particle assembly and release, the requirement of E for replication varies significantly between CoVs. Deletion of the E gene from transmissible gastroenteritis virus (TGEV), human coronavirus OC43 (HCoV-OC43), and MERS-CoV prevents viral propagation (41–43), whereas murine hepatitis virus (MHV) and SARS-CoV are only attenuated in the absence of E via an unknown mechanism (44, 45). Deleting the ORF3a and E genes from SARS-CoV and SARS-

CoV-2 eliminates viral propagation (46, 47).However, the effects of deleting only E from SARS-CoV-2 have not been reported.

Here we describe the development of a bacterial artificial chromosome (BAC) encoding SARS-CoV-2 with nanoluciferase (nLuc) in place of ORF7a/b to produce infectious reporter virus. We used this BAC system with the E gene deleted from the viral genome, ∆E SARS-CoV-2, which resulted in attenuated viral replication. Virus particles produced in the absence of E incorporated less S and were impaired for cell-free transmission. Trans-complementation of E partially rescued S incorporation and infection via virus particle spread. The primary mechanism of ∆E SARS-CoV-2 transmission was through cell fusion, which permitted evasion of antibody neutralization. ∆E SARS-CoV-2 infection resulted in greater cell surface expression of S and reorganization of the ERGIC.

Results

Design and construction of a BAC-based SARS-CoV-2 virus production system

We designed a reverse genetics platform for production of SARS-CoV-2 based on a mammalian-expression BAC encoding the complete virus genome (**Fig S1A**), similar to what has been reported with SARS-CoV and MERS-CoV (43, 48). The ORF7a/b gene was replaced with the codon-optimized nLuc reporter gene (SARS-CoV-2-nLuc). The CopyControl™ pCC1BAC vector was chosen due to its dual origin of replication that optimizes insert stability under normal bacteria propagation conditions but also permits higher DNA plasmid yield under chemical induction (49). As pCC1BAC is not designed for mammalian expression, we synthesized a mammalian expression cassette (MEC) containing the necessary *cis*-acting elements to regulate expression of the SARS-CoV-2 genome upon transfection of the BAC into mammalian cells, and to alternatively promote *in vitro* RNA synthesis from the BAC for transfection of genomic viral RNA into mammalian cells. Specifically, the human cytomegalovirus (CMV) immediate early promoter and bacteriophage T7 RNA polymerase promoter were engineered upstream of the insert site and a polyA(29) tail, the hepatitis D virus (HDV) antigenomic ribozyme, and bovine growth hormone (bGH) polyadenylation signal were engineered downstream of the insert site.

SARS-CoV-2 BAC system produces infectious virus

Production of SARS-CoV-2 was performed by transfection of the BAC into BHK cells, which are highly transfectable but not permissive to SARS-CoV-2 infection (**Fig S1B**). The transfected BHK cells were overlayed onto Vero E6 cells stably expressing human ACE2 and TMPRSS2 (Vero E6-hAT cells), which amplified virus production. SARS-CoV-2 was also produced by using the BAC as the template for *in vitro* RNA synthesis and transfecting the full-length, capped viral RNA into BHK cells (data not shown).

Vero E6-hAT cells infected with SARS-CoV-2-nLuc produced from the BAC exhibited cytopathic effects (CPE), viral plaques, and infectious titer typically observed with

SARS-CoV-2 infection (**Fig 1A-B**). Genomic RNA copies were detected in both infected cells and viral supernatant (**Fig 1C-D**). Similarly, nLuc expression was detected in infected cells (**Fig 1E**). To confirm that viral replication was occurring, RNA was isolated from infected Vero E6-hAT cells and amplified by RT-PCR using a forward primer specific to the common 5'-UTR leader sequence and reverse primers specific to each sgRNA. Agarose gel electrophoresis demonstrated that all sgRNAs were produced in cells infected with SARS-CoV-2-nLuc (**Fig 1F**). Negative stain electron microscopy (EM) and cryogenic EM (cryo-EM) of SARS-CoV-2-nLuc supernatant showed prototypical coronavirus particles of approximately 125 nm diameter and decorated with S glycoprotein trimers (**Fig 1G**). Altogether, these results demonstrate that the SARS-CoV-2 BAC system produces infectious virus particles that replicate in permissive cells.

Construction of ΔE SARS-CoV-2 BAC and E trans-complementation cell lines

To examine the role of E in SARS-CoV-2 infection, the E gene was deleted in the SARS-CoV-2 BAC. Specifically, the transcription regulatory sequence (TRS) upstream of the E gene, which is responsible for the production of the E sgRNA, and the first 186 bp of E were deleted (**Fig S2A**). The remaining 42 bp of E were left intact to preserve expression of the downstream M gene by ensuring that the M gene TRS and surrounding RNA sequence were unaltered.

To permit complementation of the deleted E gene *in trans*, stable expression BHK and Vero E6-hAT cell lines were engineered to inducibly express E. To minimize the likelihood of recombination of the trans-complemented E mRNA with the ΔE SARS-CoV-2 viral genome, the E gene was codon-optimized (coE), which removed sequence homology. To facilitate identification of cells expressing E, the codon-optimized mRuby3 fluorescent protein was linked to the N-terminus of coE by the 2A self-cleaving peptide from *Thosea asigna* virus (T2A), permitting co-expression of mRuby3 and coE (**Fig S2B**). The mRuby3-T2A-coE construct was cloned into doxycycline-inducible lentiviral vectors and transduced into BHK and Vero E6-hAT cells. Prior to each use, the cell lines were induced with doxycycline for 48h and visually confirmed by microscopy to express mRuby3, and therefore also coE (**Fig S2B**).

ΔE SARS-CoV-2 is replication competent but attenuated compared to wild-type virus

ΔE SARS-CoV-2 was produced from the BAC as described for wild-type (WT) SARS-CoV-2 to produce virus lacking E. In addition, the ΔE SARS-CoV-2 BAC was transfected into induced BHK-coE cells that were overlaid onto induced Vero E6-hAT-coE cells to produce ΔE SARS-CoV-2 trans-complemented with E protein (**Fig S2C**). A multi-passage workflow was developed to characterize ΔE SARS-CoV-2 infectivity and replication (**Fig S2D**). The initial passages (P1) of WT and ΔE SARS-CoV-2-nLuc viruses (the latter with and without E trans-complementation) were inoculated onto fresh Vero E6-hAT and Vero E6-hAT-coE cells (P2), which were subsequently passaged a third time (P3). For each passage, both the virus supernatant and the producer cells were collected and characterized.

Plaque titration revealed ΔE SARS-CoV-2 without E trans-complementation produced moderate virus titers (10^4 to 10^5 pfu/mL) in Vero E6-hAT cells, which were attenuated 2- to 3-log compared to WT SARS-CoV-2 (**Fig 2A**). Similarly, quantitative RT-PCR (qRT-PCR) of genomic RNA copies in viral supernatant showed 2- to 4-log lower levels (**Fig 2B**). Infecting fresh Vero E6-hAT cells with each virus further demonstrated a 3- to 4-log reduction in nLuc activity for ΔE SARS-CoV-2 compared to WT (**Fig 2C**). However, complementing E *in trans* did not significantly increase infectivity, genomic RNA abundance, or nLuc activity (**Fig 2A-C**).

As Vero E6-hAT cells artificially express human ACE2 and TMPRSS2, they do not represent a biologically relevant target cell of SARS-CoV-2 infection. To determine whether the observed attenuated phenotype of ΔE SARS-CoV-2 is cell type specific and to examine infection in more relevant cells, human epithelial colorectal Caco-2 cells and human respiratory epithelial Calu-3 and 16HBE cells were infected with WT and ΔE SARS-CoV-2 and assayed for nLuc activity. A similar 1.5- to 3-log reduction in infectivity was observed for ΔE SARS-CoV-2 compared to WT in Vero E6, Caco-2, and Calu-3 cells as was observed in Vero E6-hAT cells (**Fig 2D**).

Surprisingly, while ΔE SARS-CoV-2 had similar infectivity in 16HBE cells as in the other cell lines, WT SARS-CoV-2 infectivity was about 1-log lower than ΔE SARS-CoV-2 infectivity (**Fig 2D**). To investigate whether 16HBE cells had lower expression of ACE2, all of the cell lines were stained for human ACE2 and imaged for immunofluorescence (**Fig 2E**). Vero E6-hAT cells, as expected, showed a high level of ACE2 expression, commensurate with the observed infectivity of SARS-CoV-2. The human cell lines showed lower levels of ACE2 expression than Vero E6-hAT cells, with 16HBE cells having the least ACE2 expression. Parental Vero E6 cells, which had relatively high WT SARS-CoV-2 infectivity, showed low surface expression of ACE2.

To determine if increased ACE2 expression could rescue WT SARS-CoV-2 infectivity in 16HBE cells, they were transduced with a lentiviral vector encoding human ACE2, resulting in a similar level of ACE2 cell surface expression as in Vero E6-hAT cells (**Fig 2E**). Both WT and ΔE SARS-CoV-2 showed increased infectivity in 16HBE-ACE2 cells compared with parental 16HBE cells (**Fig 2D**); however, while ΔE SARS-CoV-2 infectivity was about 1-log higher in 16HBE-ACE2 cells, WT SARS-CoV-2 infectivity was enhanced 3.5-log in 16HBE-ACE2 cells. Collectively, these data demonstrate that deletion of E from SARS-CoV-2 results in attenuated viral infectivity across multiple cell types.

ΔE SARS-CoV-2 virus infection produces expected sgRNAs and does not recombine with trans-complemented coE

Attenuation rather than loss of infectivity of ΔE SARS-CoV-2 could be explained by restoration of E gene expression, compensatory mutations, or a lack of expression of other viral genes due to the E gene deletion. To confirm that the ΔE SARS-CoV-2 genome had not been altered through passaging, RNA was isolated from passage 3 (P3) virus and sequenced. The E gene deletion confirmed in the ΔE SARS-CoV-2 BAC was also observed in P3 virus, and no additional mutations were observed in the sequenced region, which spanned from the last 437 bp of S through the end of ORF6.

To confirm that all sgRNAs except E are produced by ∆E SARS-CoV-2, RNA from infected cells was isolated, RT-PCR amplified with sgRNA-specific primers, and visualized by agarose gel electrophoresis. For each virus, the amount of cDNA added to each RT-PCR reaction was normalized to the relative abundance of ORF1a compared to WT virus. All sgRNAs except E were detected in ∆E SARS-CoV-2 infected cells with similar relative abundance as for WT SARS-CoV-2, with and without coE trans-complementation (**Fig 3A**). E sgRNA was not detected after ∆E SARS-CoV-2 infection with or without coE. To further confirm a lack of E expression during ∆E SARS-CoV-2 replication, RNA isolated from producer cells and supernatants from all three passages of WT SARS-CoV-2 or ∆E SARS-CoV-2 with and without coE was examined by qRT-PCR. While WT SARS-CoV-2 infection produced E sgRNA in cells and virus, no E sgRNA was detected with ∆E SARS-CoV-2 infection with or without coE (**Fig 3B**).

The lack of appreciable rescue of ∆E SARS-CoV-2 infectivity by coE trans-complementation could be due to a lack of coE expression, despite mRuby3 expression in induced coE cells. Enumeration of coE copies by qRT-PCR demonstrated that coE was expressed across all three passages in trans-complemented cells, albeit at a level 2- to 4-log lower than endogenous E detected during WT SARS-CoV-2 infection (**Fig 3C**, left). To determine if the level of coE mRNA expression was influenced by SARS-CoV-2 infection, coE copies were enumerated in RNA isolated from induced Vero E6-hAT-coE cells that were mock infected or infected with WT or ∆E SARS-CoV-2. The expression level of coE was similar in induced Vero E6-hAT-coE cells without infection or with infection by WT or ∆E SARS-CoV-2 (**Fig S3**). Importantly, coE was not detected in ∆E SARS-CoV-2 virus produced in coE-expressing cells (**Fig 3C**, right), further confirming a lack of recombination of coE mRNA with the ∆E SARS-CoV-2 viral genome.

∆E SARS-CoV-2 is defective for virus production and spread and is partially rescued by E trans-complementation

While ΔE SARS-CoV-2 infectivity was not significantly rescued by coE trans-complementation (**Fig 2A-C**), other characteristics of this mutant virus were rescued by E expression. While performing plaque titration of the viruses, we observed that ΔE SARS-CoV-2 generated small, pinprick-like plaques compared to large, distinct WT plaques (**Fig 4A**). In contrast, titration in cells expressing E resulted in ΔE SARS-CoV-2 plaques that matched WT plaques regardless of whether they were produced in cells expressing E. Of note, it did not matter if ΔE SARS-CoV-2 was originally produced in cells expressing E, as all ΔE SARS-CoV-2 viruses produced small plaques when inoculated onto cells lacking E. Similarly, infecting Vero E6-hAT cells (lacking E expression) with ΔE SARS-CoV-2 produced in cells with or without E expression showed no appreciable difference in infectivity (**Fig S4A**). Conversely, ΔE SARS-CoV-2 infection of Vero E6-hAT cells expressing E resulted in a 20-fold increased infectivity compared with ΔE SARS-CoV-2 infection of Vero E6-hAT cells without E (**Fig S4B**). Thus, rescue of ΔE SARS-CoV-2 infectivity is dependent upon the presence of E in target cells, not in producer cells.

In addition to ΔE SARS-CoV-2 having reduced virus particle production (**Fig 2B**), the particles themselves differ from WT SARS-CoV-2 virus particles. While most WT virions visualized by negative stain EM and cryo-EM were broadly decorated with S trimers, most ΔE SARS-CoV-2 virions displayed little or no S and often appeared misshapen (**Fig 4B**). Production of ΔE SARS-CoV-2 in cells expressing E resulted in a mixed phenotype, with some WT-like particles but also a population of defective particles similar to those produced in cells without E expression. A Western blot of purified viruses showed less incorporation of S in ΔE SARS-CoV-2 virions compared to WT virions (**Fig 4C**).

Examining nLuc expression of cells infected with WT or ΔE SARS-CoV-2 virus by immunofluorescence microscopy revealed that WT and ΔE viruses propagate differently. Cells infected with WT SARS-CoV-2 showed some contiguous patches of nLuc-expressing cells that were suggestive of cell-to-cell spread, as has been previously

reported (50, 51), but predominantly consisted of scattered individual cells or small numbers of cells expressing nLuc that were consistent with particle-based spread (**Fig 4D**). In contrast, cells infected with ∆E SARS-CoV-2 showed little evidence of particle-based spread but instead contained large islands of nLuc-expressing cells that appeared to be syncytia. Interestingly, nuclear staining of these islands of nLuc-expressing cells showed a distinct “eye of the hurricane” pattern of aggregated nuclei with an empty center, which was not observed with WT SARS-CoV-2 infection. ∆E SARS-CoV-2 infection of E-expressing cells produced an increase in particle-based spread but also appreciably enhanced cell-to-cell transmission (**Fig 4E**). Similarly, WT SARS-CoV-2 infection of cells expressing E also showed an increase in cell-to-cell spread. Collectively these data demonstrate that ∆E SARS-CoV-2 is defective for virus particle production and particle-based spread, is transmitted primarily cell-to-cell, and is partially rescued by E trans-complementation.

S neutralizing antibody inhibits SARS-CoV-2 virus particle spread but not cell-to-cell transmission

Neutralizing antibodies (NAbs) directed against S can effectively inhibit SARS-CoV-2 infection (52, 53). Protection of viral infections by NAbs appears to be predominantly based on inhibiting cell-free virus spread and targeting surface-exposed antigen on infected cells (53), which is circumvented by cell-to-cell virus transmission (51, 54–56) Since ∆E SARS-CoV-2 appears to spread primarily cell-to-cell, we examined whether a NAb could prevent ∆E SARS-CoV-2 infection. The LY-CoV555 (bamlanivimab) NAb was effective at neutralizing USA-WA1/2020 SARS-CoV-2 (57–59) with an effective concentration to reduce infection by 50% (EC_{50}) of 0.01 µg/mL in Vero E6-hAT cells (59). Vero E6-hAT cells were infected with WT or ∆E SARS-CoV-2-nLuc that had been pre-incubated for 1 h with NAb at the reported EC_{50}, EC_{90}, or 10 times the EC_{90} dose or left untreated. After 24 h the cells were assayed for nLuc activity (**Fig 5A**). The lowest dose of NAb was sufficient to reduce WT SARS-CoV-2 infectivity 10-fold, with no nLuc activity detected at the higher doses. In comparison, ∆E SARS-CoV-2 infectivity was reduced only 2-fold at the lowest dose and nLuc activity was still detectable at the higher doses, albeit reduced 100- and 500-fold (**Fig 5A**).

To directly compare WT and ΔE SARS-CoV-2 cell-to-cell transmission, a method was needed to permit initial infection of cells but to inhibit subsequent cell-free infection while allowing cell-to-cell spread. Thus, Vero E6-hAT cells were infected with WT or ΔE SARS-CoV-2-nLuc for 1 h before treatment with NAb and assayed for nLuc activity after 24 h (**Fig 5B**). As the EC_{50} dose of NAb did not inhibit WT or ΔE SARS-CoV-2 when applied post-inoculation (data not shown), only the EC_{90} and 10 times EC_{90} doses were used. Like what was observed with NAb pre-treatment, WT SARS-CoV-2 infectivity was reduced 10- and 100-fold compared to no NAb treatment, whereas ΔE SARS-CoV-2 infectivity was only reduced 1.5- and 3-fold (**Fig 5B**).

We hypothesized that the difference in NAb efficacy at inhibiting WT and ΔE SARS-CoV-2 infectivity after virus challenge was due to the relative contribution of virus particle spread to overall infectivity for each virus but that both viruses retained the ability to transmit cell-to-cell. To confirm this, nLuc expression was visualized in cells with and without NAb pre-treatment and infected with viruses (**Fig 5C**). Without NAb treatment, both WT and ΔE SARS-CoV-2 exhibited similar patterns of cell-to-cell and cell-free spread as shown in **Fig 4D**. Treating with increasing doses of NAb inhibited particle-based spread but preserved cell-to-cell spread by both WT and ΔE SARS-CoV-2 (**Fig 5C**). At the highest dose of NAb (1.0 μg/mL, 10 times EC_{90}) no particle-based spread was apparent for either WT or ΔE SARS-CoV-2. Altogether, these results demonstrate that NAb treatment inhibits SARS-CoV-2 virus particle spread but not cell-to-cell transmission and that ΔE SARS-CoV-2 is transmitted primarily cell-to-cell.

SARS-CoV-2-mediated cell fusion is enhanced by E expression in infected target cells

Inhibiting SARS-CoV-2 virus particle spread while preserving cell-to-cell spread through high dose NAb treatment affords the ability to directly compare WT and ΔE SARS-CoV-2 cell-to-cell transmission without the confounding effects of potentially unequal virus particle spread. While the pattern of infected cells during high dose NAb treatment suggests transmission is occurring cell-to-cell via syncytia formation (**Fig 5C**), it is also

possible that localized virus particle spread without cell fusion occurs. To determine whether SARS-CoV-2 transmission with high NAb concentrations occurs through syncytia formation, we employed a bimolecular fluorescence complementation (BiFC) cell fusion reporter system, in which the linked Renilla luciferase (rLuc) and enhanced green fluorescent protein (eGFP) genes are split into N- and C-terminal fragments, NrLuc-eGFP and rLuc-eGFPC (60). Stable expression of either the NrLuc-eGFP or rLuc-eGFPC fragment was accomplished by transducing Vero E6-hAT cells with a lentiviral vector encoding one of the fragments, generating Vero E6-hAT-N and Vero E6-hAT-C cell lines. Both lines were co-cultured 1:1, infected with SARS-CoV-2-nLuc at a low multiplicity of infection (MOI=0.01) for 1 h, and treated with NAb for 24 h. Then the cells were fixed and imaged for nLuc expression by fluorescence microscopy (**Fig S5A**). Fusion of adjacent Vero E6-hAT-N and Vero E6-hAT-C cells resulted in the reconstitution of rLuc and eGFP and produced green fluorescence. Infected cells, which were positive for nLuc expression, were also positive for reconstituted eGFP expression, indicating that SARS-CoV-2 transmission in the presence of a high NAb concentration occurs through cell fusion (**Fig S5B**).

To compare cell fusion induced by WT and ΔE SARS-CoV-2, Vero E6-hAT cells with or without E expression were infected with WT or ΔE virus for 1 h, treated with NAb for 24h, fixed, and stained for nLuc expression (**Fig 6A**). Infection with WT SARS-CoV-2 resulted in larger syncytia than ΔE SARS-CoV-2 in Vero E6-hAT cells (**Figs 6B, S5B**). Syncytia size was enhanced for both viruses in Vero E6-hAT-coE cells expressing E. Interestingly, the “eye of the hurricane” aggregated nuclei structures observed with ΔE SARS-CoV-2 infection without NAb treatment (**Fig 4D**) were also present during WT SARS-CoV-2 infection with NAb treatment (**Fig 6A**). Collectively, these data suggest virus-mediated cell fusion is enhanced by E expression in infected target cells.

Lack of E during SARS-CoV-2 infection results in greater S cell surface expression and ERGIC reorganization

Prior work has demonstrated that expression of SARS-CoV-2 S protein in cells results in its expression on the cell surface (38, 61). Co-expressing E with S causes S to be

predominantly retained within the ERGIC to facilitate virus particle assembly (38). Given our observation that fewer S trimers were incorporated into ΔE SARS-CoV-2 virus particles compared with WT particles (**Fig 4B**), we hypothesized that the lack of E expression with ΔE SARS-CoV-2 infection results in less S retention within the ERGIC and increased expression at the cell surface. To examine S localization during WT and ΔE SARS-CoV-2 infection, Vero E6-hAT cells were infected with WT or ΔE SARS-CoV-2 and fixed after 24 h. The cells were stained prior to permeabilization with anti-S primary and red fluorescent secondary antibodies to detect cell surface expression. After permeabilization, the cells were stained with anti-S primary and green fluorescent secondary antibodies to detect total (surface and internal) expression. After imaging via confocal microscopy, green fluorescence that co-localized with red fluorescence (representing cell surface expressed S that was labeled with both sets of antibodies) was masked to visualize distinct populations of surface (red) and internal (green) S (**Fig 7A**). Infection with ΔE SARS-CoV-2 resulted in increased S surface expression compared with WT virus (**Fig 7B**). While a high degree of variability was observed in the proportion of surface-expressed S in ΔE SARS-CoV-2-infected cells resulting in a lack of statistical significance, there was nonetheless a trend for higher S surface expression in some cells infected with ΔE SARS-CoV-2 compared to WT virus.

Different localization patterns of internal S in cells infected with WT or ΔE SARS-CoV-2 were observed (**Fig 7A**). While most internal S in cells infected with WT SARS-CoV-2 appeared in centralized, perinuclear structures consistent with ERGIC localization, S inside ΔE SARS-CoV-2-infected cells was more diffuse, raising the question of whether S in cells infected with ΔE SARS-CoV-2 was retained within the ERGIC. To test this, Vero E6-hAT cells were infected with WT or ΔE SARS-CoV-2 for 24 h and stained for S and the canonical ERGIC marker protein ERGIC-53 (**Fig 8A**). Cells infected with WT virus exhibited the same ERGIC-53 staining pattern as uninfected cells, with S co-localizing with ERGIC-53. In contrast, cells infected with ΔE SARS-CoV-2 also exhibited strong co-localization of S and ERGIC-53, but the ERGIC structure was reorganized, appearing more diffuse compared to uninfected cells or cells infected with WT virus. Within ΔE virus-mediated syncytia, the center of the “eye of the hurricane” aggregated

nuclei structure was filled with diffuse ERGIC-53 co-localized with S. To determine if this altered ERGIC organization was due to SARS-CoV-2-induced syncytia or specific to ΔE SARS-CoV-2 infection, WT and ΔE syncytia were directly compared (**Fig 8B**). Unlike the diffuse ERGIC observed with ΔE SARS-CoV-2 syncytia, WT virus syncytia retained multiple dense ERGIC structures. Altogether, these data demonstrate that a lack of E during SARS-CoV-2 infection results in greater S cell surface expression and reorganization of the ERGIC.

Discussion

Previous studies have shown that TGEV, HCoV-OC43, and MERS-CoV lacking E are unable to replicate (41–43). In contrast, MHV and SARS-CoV are attenuated without E (44, 45), which we also observed for ΔE SARS-CoV-2 in Vero-E6-hAT cells and multiple human epithelial cell lines. We showed that ΔE SARS-CoV-2 attenuation was due to reduced infectious particle production and increased cell-to-cell transmission (**Fig 9**). Plaque titration of ΔE SARS-CoV-2 demonstrated fewer and much smaller plaques compared to the large, distinct plaques observed with WT virus, which was also observed for MHV and SARS-CoV (44, 45). Increased cell surface expression of S was observed for ΔE SARS-CoV-2, which led to significantly reduced virus production and release from the ERGIC pathway and any virions that were produced had little incorporation of S. This was expected given the previously reported roles of CoV E in virion assembly and release (36–38) . In addition, transfection studies showed that SARS-CoV-2 E expression slows down the secretory pathway, inducing retention of glycoproteins in the ERGIC, including S (38) . We hypothesized that a lack of intracellular S expression could lead to its expression at the cell surface, which was true to an extent, but surface S localization was variable. Unexpectedly, ΔE SARS-CoV-2 led to changes in ERGIC morphology.

ΔE SARS-CoV-2 infectivity and virus particle production and transmission by trans-complementation of E was partially rescued. A primary factor in this limited rescue is likely the expression level of trans-complemented E, which had 2-3-log lower mRNA abundance in infected cells versus endogenous E sgRNA during WT virus infection. While SARS-CoV-2 has been shown to inhibit host protein synthesis during translation and mRNA nuclear export (62–64), the abundance of trans-complemented E mRNA was similar in uninfected and infected cells, suggesting that the virus did not inhibit mRNA production or stability. However, cells trans-complemented with E had lower mRuby3 protein expression after SARS-CoV-2 infection, suggesting virus-induced host protein inhibition reduced trans-complemented E protein expression levels. Optimization

of the trans-complementation system to overcome these limitations should improve rescue.

The variability in E dependency across CoVs suggests E performs multiple roles in virus assembly and release (65), some of which are crucial and others that may be dispensable or that can be substituted for by other viral proteins (66). We confirmed that attenuation of ΔE SARS-CoV-2 was authentic and not due to reconstitution of the E gene or emergence of compensatory mutations. Examining production of sgRNAs by ΔE virus with and without E trans-complementation showed that all sgRNAs except E sgRNA are produced with similar abundance to WT. This demonstrates that attenuated ΔE SARS-CoV-2 infectivity is not due to a defect in viral RNA synthesis but suggests the replication defect occurs after RNA synthesis. While deleting either the E gene or the ORF3 gene in SARS-CoV reduced but did not eliminate viral titers, deletion of both E and ORF3a abrogated SARS-CoV and SARS-CoV-2 replication, indicating that ORF3a can substitute for some functionality of E (46, 47). This would make both viral proteins potential candidates for compensatory mutations to overcome replication defects introduced by the deletion of E. However, no mutations were observed after three passages of ΔE SARS-CoV-2.

While higher surface expression of S during ΔE SARS-CoV-2 infection was anticipated to promote increased cell fusion compared to WT infection, we also observed that trans-complementation of E enhanced cell fusion, including with WT SARS-CoV-2 infection. The C-terminus of E contains a PSD-95/Dlg/ZO-1 (PDZ)-binding motif, facilitating interactions of E with various PDZ-containing host proteins, including Zona Occludens-1 (ZO1) and Proteins Associated with Lin Seven 1 (PALS1), which are key regulators of tight junction (TJ) formation and epithelial monolayer integrity (67, 68). Further, E expression has been shown to downregulate expression of TJ proteins Occludin and Claudin-4 (69). Disruption of TJs and epithelial monolayer integrity could facilitate cell fusion. Alternatively, the viroporin activity of E, by altering Ca^{2+} homeostasis, could promote syncytia formation, which has been shown to be dependent upon Ca^{2+}

oscillations (70–72). Further studies are needed to elucidate how E expression enhances virus-induced cell fusion.

It is generally agreed that CoV assembly occurs in or near the ERGIC but trafficking of nascent virions from the ERGIC to extracellular space is less certain. Different pathways may be utilized and/or altered by different CoVs, including the Golgi secretory pathway, the endosome recycling compartment, or lysosomal exocytosis (73–76). Fragmentation of the Golgi and its translocation to the center of virus-induced syncytia was previously observed with MHV (77). Fluorescence imaging also noted Golgi fragmentation during late SARS-CoV-2 infection, when M, S, and E proteins were expressed and after recruitment of the lysosomal marker LAMP1 to the Golgi/ERGIC, likely due to fusion of lysosomes with ERGIC membranes (78). However, we only observed ERGIC fragmentation after infection with ΔE SARS-CoV-2, suggesting that this phenomenon is transient during late SARS-CoV-2 infection and is enhanced if E is not present.

SARS-CoV-2 infection has been shown to result in an accumulation of autophagosomes but inhibition of cargo degradation through reduced autophagic flux, processes which involve E and M and which may lead to virus particle release (79, 80). The localization of M to ERGIC-derived autophagosomes is dependent upon expression of E, without which M localizes to the Golgi (81–83). It could be envisioned that without E, accumulation of M – and perhaps nascent virions – in the Golgi/ERGIC could promote the observed fragmentation and translocation, as well as alter the pathway through which virions are released. As E has been described in slowing down the secretory pathway (38), its absence could accelerate virus-induced processes within the secretory compartments. Additional studies investigating SARS-CoV-2 virus particle assembly and trafficking are needed to examine how the presence or absence of E alters these processes as well as the cellular secretory system.

Materials and Methods

Biosafety statement

All SARS-CoV-2 virus production and infections were performed at biosafety level 3 in the Regional Biocontainment Laboratory at the University of Pittsburgh Center for Vaccine Research.

SARS-CoV-2 BAC

The SARS-CoV-2 USA-WA1/2020 viral genome was obtained as 7 individual cDNA fragments cloned within pUC57 or pCC1BAC via a Materials Transfer Agreement from the University of Texas Medical Branch (84), with and without replacement of the ORF7a/b gene by the mNeonGreen (mNeon) reporter gene. The mNeon reporter gene in fragment 7 was replaced via Gibson cloning with the codon-optimized nLuc gene from a reporter lentiviral genome (pNL4-nLucCO-6ATRi-BAL) that we had previously produced (85).

SARS-CoV-2 genome fragments 1-4 and fragments 5-7 were each assembled using the Golden Gate Assembly kit per the manufacturer's instructions (NEB), with type IIB restriction enzymes BsaI-HFv2 and Esp3I, respectively. A MEC was produced via gene synthesis (GenScript), consisting of the CMV and T7 promoters upstream of the first 351 bp of the SARS-CoV-2 USA-WA1/2020 genome (from the start of the 5' UTR up to the unique BsiWI restriction site within the nsp1 gene) and the last 1,398 bp of the viral genome (from the unique XhoI restriction site within the nucleocapsid gene through the end of the 3' UTR) followed by a polyA(29) tail, HDV ribozyme, and bovine growth hormone polyadenylation signal sequence. This MEC was cloned into pCC1BAC via NotI/BamHI restriction cloning to produce a mammalian expression BAC (pBAC), which was subsequently digested with BsiWI and XhoI and incubated with digested fragments 1-4 (BsiWI restriction enzyme) and fragments 5-7 (XhoI restriction enzyme) together with T4 DNA ligase to produce the full SARS-CoV-2 genome with and without an nLuc reporter. To facilitate assembly of the full-length SARS-CoV-2 genome into the BAC, the 5' end (the first 351 bp of the genome consisting of the 5'-UTR and the N-terminal of the

nsp1 gene through the unique BsiWI restriction site) and the 3' end (the last 1,398 bp of the genome from the unique XhoI restriction site in nucleocapsid through the 3'-UTR) of the viral genome were synthesized as part of the MEC. The full SARS-CoV-2 genome sequence within the BAC was verified by Sanger sequencing.

ΔE SARS-CoV-2 BAC

The E TRS and the first 186 bp of the E gene were deleted from the SARS-CoV-2 genome to produce ΔE SARS-CoV-2 that lacked expression of E but preserved the expression of the downstream M gene and all subsequent genes. Briefly, portions of fragments 6 and 7 from UTMB were PCR amplified and Topo cloned into pCR2.1-TOPO (ThermoFisher Scientific). Deletion of E was performed by Gibson cloning. The fragments were then assembled as described above. The full ΔE SARS-CoV-2 genome sequence within the BAC was verified by Sanger sequencing.

Inducible SARS-CoV-2 E expression constructs

pLVX-TetOne-Puro-mRuby3co-T2A-coE was produced by gene synthesis (GenScript) of the codon-optimized versions of mRuby3 and the SARS-CoV-2 USA-WA1/2020 E gene linked by the T2A peptide, which was cloned by EcoRI/AgeI restriction cloning into the pLVX-TetOne-Puro-hAXL plasmid (Addgene). A variation replacing the puromycin resistance gene in the pLVX-TetOne-Puro vector with the NeoR/KanR/G418 resistance gene from pIRES (Takara Bio) via Gibson cloning produced pLVX-TetOne-G418-mRuby3co-T2A-coE.

Cell fusion/syncytia reporter constructs

The N- and C-terminal fragments of the split renilla luciferase and enhanced green fluorescent protein fusion (Split-rLuc-eGFP) BiFC reporter were cloned from pCG-NrLuc-eGFP and pCG-rLuc-eGFPC, respectively (60), into the XbaI/SalI digested pLenti-CMV-Hygro-ACE2 plasmid (Addgene) via Gibson cloning to produce pLenti-CMV-Hygro-NrLuc-eGFP and pLenti-CMV-Hygro-rLuc-eGFPC.

Cells

Vero E6 cells are AGM (*Cercopithecus aethiops*) kidney cells (ATCC), BHK cells are Syrian hamster (*Mesocricetus auratus*) kidney cells, HEK 293T and 293F cells are human epithelial cells, Calu-3 cells are human lung adenocarcinoma cells, Caco-2 cells are human colorectal adenocarcinoma cells, and 16HBE14o- cells (16HBE) are human bronchial epithelial cells. These cells were grown in Dulbecco's Modified Eagle Medium (DMEM) containing 10% or 20% (Caco-2) fetal bovine serum (FBS; Atlanta Biologicals), 100 U/ml penicillin, 100 µg/ml streptomycin, and 2 mM L-glutamine (PSG; ThermoFisher Scientific), termed DMEM-10 medium, at 37° C and 5% CO_2. 293F cells were maintained at 37° C with 5% CO_2 in FreeStyle 293 Expression Medium (Thermo Fisher) supplemented with penicillin and streptomycin (Gibco). Vero E6-hAT cells were obtained from BEI Resources and grown in DMEM-10 supplemented with 10 µg/ml puromycin (Invivogen).

16HBE-ACE2 cells were produced by stable transduction of 16HBE cells with pLenti-CMV-Hygro-ACE2 lentivirus and maintained in DMEM-10 supplemented with 500 µg/ml hygromycin (Invitrogen). Vero E6-hAT-NrLuc-eGFP (Vero E6-hAT-N) and Vero E6-hAT-rLuc-eGFPC (Vero E6-hAT-C) cells were produced by stable transduction of Vero E6-hAT cells with pLenti-CMV-Hygro lentivirus encoding the N-terminal or C-terminal fragment of the Split-rLuc-eGFP fusion reporter gene, respectively, and maintained in DMEM-10 supplemented with 10 µg/ml puromycin and 500 µg/ml hygromycin.

BHK-coE cells were produced by stable transduction of BHK cells with pLVX-TetOne-Puro lentivirus encoding mRuby3-T2A-coE and maintained in DMEM-10 supplemented with 3 µg/ml puromycin. Vero E6-hAT-coE cells were produced by stable transduction of Vero E6-hAT cells with pLVX-TetOne-G418-mRuby3-T2A-coE lentivirus and maintained in DMEM-10 supplemented with 10 µg/ml puromycin and 500 µg/ml G418 (Gibco). Vero E6-hAT-N-coE and Vero E6-hAT-C-coE cells were produced by stable transduction of Vero E6-hAT-N and Vero E6-hAT-C cells, respectively, with pLVX-TetOne-G418-mRuby3-T2A-coE lentivirus and maintained in DMEM-10 supplemented with 10 µg/mL puromycin, 500 µg/ml hygromycin, and 500 µg/ml G418. TetOne-mediated expression of mRuby3-T2A-coE was induced with 100 ng/ml doxycycline (Thermo Scientific) for 48

h prior to use, which was maintained throughout the course of the experiment. Expression of mRuby3-T2A-coE was visually confirmed by widefield epifluorescence microscopy prior to use.

Production of lentiviruses

pLenti and pLVX viruses were produced by Lipofectamine 2000 (ThermoFisher Scientific) transfection in 293T cells with the pCAGGS-PAX2 lentiviral packaging plasmid and the pL-VSV-G plasmid. Virus was harvested 48 h later, centrifuged at 2000 x g for 20 m, filtered through a 0.45 µm polyethersulfone (PES) filter (Millipore), aliquoted, and frozen at -80° C.

Production of SARS-CoV-2 virions

Transfection of 20 µg viral cDNA into 4 x 10^6 BHK cells in a 100 mm dish was performed with Lipofectamine 2000. The medium was removed after 24 h and the cells were split 1:2, overlaid onto two 100 mm dishes each of 5 x 10^6 Vero E6-hAT cells, and incubated for 3 days. Supernatants were centrifuged at 2000 x g for 20 m, filtered through a 0.45 µm PES filter, and aliquoted frozen at -80° C or lysed in TRIzol-LS (ThermoFisher Scientific). For ΔE SARS-CoV-2 virus production, transfections were also performed in BHK-coE and Vero E6-hAT-coE cells induced with doxycycline.

nLuc assay

nLuc from transfected or infected cells was measured by lysing cells in Nano-Glo Luciferase Assay Buffer (Promega), incubation with Nano-Glo Luciferase Assay Substrate (Promega), and detection on a BioTek Synergy2 Multi-Detection Microplate Reader.

RT-PCR

RNA was isolated from TRIzol-LS-treated virus or TRIzol-treated cell lysates as previously described (86). RT-PCRs were performed using primers shown in **Table 1** and PCR reactions were run on an agarose gel for visualization. Quantitative RT-PCRs

were performed using primers and probes listed in **Table 1** with plasmids used as standards and run on a Bio-Rad CFX96 Real-Time PCR System.

Plaque assay

Vero E6-hAT cells were plated at 1 x 10^6 cells/well overnight in 6-well plates. Virus was diluted in 10-fold serial dilutions in OptiMEM medium (ThermoFisher Scientific) + 2% FBS. Medium was removed from cells and 200 µl virus dilutions were added in duplicate to wells and incubated at 37° C, 5% CO_2 for 1 h, with plates tilted every 15 m. The virus was removed from all wells and cells were washed once with phosphate buffered saline (PBS, Gibco) before overlay with 3 ml of 1.25% Avicel (Millipore Sigma) in EMEM medium (Quality Biological) with 10% FBS, PSG, and Non-Essential Amino Acids (Gibco). Plates were incubated 2-5 days and the Avicel was removed in PBS. Cells were fixed in 10% formalin for 24 h at room temperature (RT). Wells were washed with PBS and stained with 0.2% crystal violet in 25% methanol for 15 m at RT. Stained plates were washed in water to remove excess stain and allowed to air dry overnight. Plaques were imaged on a flatbed scanner and counted.

EM

SARS-CoV-2 virions were fixed in equal volume 4% paraformaldehyde (PFA) with 10 mM HEPES for 48 h at 4° C, ultracentrifuged through a 20% sucrose cushion in NTE buffer (100 mM NaCl, 10 mM Tris-HCl, 1 mM EDTA, pH 7.6) for 2.5 h, 4° C at 117,250 x g, and resuspended in NTE buffer. For negative stain EM, 3 µL of sample was applied to a freshly glow-discharged continuous carbon copper grid and stained with 1% uranyl acetate solution. The grids were then inserted into a Tecnai TF20 electron microscope (Thermo Fisher Scientific, MA, USA), equipped with a field emission gun and images captured using an XF416 CMOS camera (TVIPS GmbH, Gilching, Germany) to assess particle assembly and presence of Spike. For cryo-EM, 3 µL of sample was applied to a freshly glow-discharged Quantifoil R2/1 grid (Quantifoil Micro Tools GmbH, Großlöbicha, Germany) and then blotted and plunge-frozen with a Vitrobot Mk 4 (TFS). Grids were mounted on a Krios 3Gi cryo-electron microscope operating at 300 kV and equipped with a Falcon 4i direct electron detecting camera (TFS). Images were collected in

electron counting mode under the control of the TFS EPU software using a total dose of ~30 e/Å^2. A magnification of 85,000x was used, correspond to 1.51 Å per pixel at the sample.

Western blot

Vero E6-hAT cells were seeded at 15 x 10^6 cells/dish overnight in 150 mm dishes and infected with virus (MOI=0.05). After 24 h, supernatants were centrifuged at 2000 x g for 20 m, filtered through a 0.45 µm PES filter, supplemented with 10 mM HEPES, ultracentrifuged through a 20% sucrose cushion in NTE buffer for 2 h, 4° C at 117,250 g, resuspended overnight at 4° C in 300 µl RIPA buffer (Boston BioProducts) supplemented with complete protease inhibitor (Roche), aliquoted, and frozen at -20° C. Concentrated supernatants were combined with 4X Laemmli sample buffer (Bio-Rad) and 355 mM 2-Mercaptoethanol (Sigma-Aldrich), and denatured at 95° C for 5 m. Samples were loaded onto a pre-cast 4-15% gradient TGX polyacrylamide gel (Bio-Rad) at equal amount of total protein as determined by Lowry assay (Bio-Rad) and subjected to SDS-PAGE gel electrophoresis at 150 V for 1 h. Proteins were transferred to a nitrocellulose membrane (Millipore) using a wet-electroblotting transfer chamber (Bio-Rad) in Towbin buffer containing 20% methanol and 0.4% SDS (Boston BioProducts) at 75 V, 4° C for 1 h. Membranes were washed in Tris-buffered saline (TBS, Boston BioProducts), blocked in Intercept TBS blocking buffer (LI-COR) for 1 h at RT, and incubated with primary antibodies against S (mouse α-S GTX632604, Genetex, 1:1000) and N (rabbit α-N 200-401-A50, Rockland, 1:3000) diluted in Intercept TBS blocking buffer supplemented with 0.2% Tween-20 (T-20 diluent) overnight at 4° C. Membranes were washed 4 times for 5 m with TBS supplemented with 0.2% Tween-20 (TBS-T), incubated with secondary antibodies (donkey α-mouse IRDye 680LT and donkey α-rabbit IRDye 800CW , LI-COR, 1:20,000) diluted in T-20 diluent for 1 h at RT, washed 4 times for 5 m with TBS-T, and rinsed with TBS. Membranes were developed on a LI-COR Odyssey Clx imager with ImageStudio software using default acquisition settings and quantified with Fiji/ImageJ (87).

Neutralizing antibody assays

DNA encoding SARS-CoV-2 S NAb LY-CoV555 heavy- and light-chain variable domain genes were synthesized by IDT and cloned into a modified pVRC to produce full length human IgG1 antibodies as previously described (88) . Recombinant LY-COV555 was produced by polyethylenimine (PEI) facilitated, transient transfection of 293F cells that were maintained in FreeStyle 293 Expression Medium. Transfection complexes were prepared in OptiMEM and added to cells. Five days post-transfection supernatants were harvested, clarified by low-speed centrifugation, and incubated overnight with Protein Agarose Resin (GoldBio). The resin was collected in a chromatography column, washed with a column volume of 10 mM tris(hydroxymethyl)aminomethane-HCl (TRIS), 150 mM NaCl at pH 7.5, and eluted in 0.1M Glycine (pH 2.5) which was immediately neutralized by 1M TRIS, (pH 8.5). Antibodies were then dialyzed against PBS (pH 7.4). Vero E6-hAT cells were plated at 1.25 x 10^5 cells/well overnight in 24-well plates. In one set of experiments, virus was pre-treated with NAb for 1 h at 37° C prior to infecting cells in duplicate wells for 24 h. In a second set of experiments, cells were infected with virus for 1 h before virus was removed from all wells and cells were washed once with PBS, fed with DMEM-10 supplemented with NAb, and incubated for 24 h. For both sets of experiments infection was measured by nLuc assay.

Immunofluorescence microscopy

Unless otherwise indicated below for specific experiments, standard immunofluorescence microscopy sample preparation was as follows: Cells were seeded into 35 mm glass-bottom dishes (MatTek) and incubated until near confluence, overnight to 48 h. Cells were fixed with 4% PFA for 24 h at 4° C, permeabilized with 0.1% Triton X-100 (ThermoFisher Scientific) for 15 m at RT, blocked with 5% normal goat serum (Invitrogen) for 1 h at RT, incubated with primary antibody for 1 h at RT, incubated with secondary antibody for 1 h at RT, counterstained with Hoechst 33342 (1:2000, ThermoFisher Scientific) for 15 m at RT, and mounted with 1.5 glass coverslips. Blocking and immunofluorescence staining/wash buffers contained 0.5% bovine serum albumin (ThermoFisher Scientific) and 1% glycine (Millipore Sigma) in PBS.

For ACE2 cell surface expression, cells were counterstained with Hoechst 33342 prior to fixation with 2% PFA for 20 m at RT. No permeabilization was performed. Primary antibody (mouse α-ACE2 MAB9332, R&D Systems, 1:100) was incubated for 24 h at 4° C. Secondary antibody (goat α-mouse-AlexaFluor488, Invitrogen, 1:500) was incubated for 1 h at RT. Confocal laser scanning microscopy was performed with a Nikon A1 microscope equipped with a motorized piezo Z stage and images were analyzed with Nikon Elements.

For nLuc expression, Vero E6-hAT and induced Vero E6-hAT-coE cells were seeded at 3 x 10^5 cells/well overnight into either 6-well plates or MatTek dishes, infected with virus for 1 h, washed with PBS, and fed with DMEM-10, which in some experiments was supplemented with NAb. After 24 h, cells were fixed and prepared according to the above standard protocol with primary (mouse α-nLuc MAB10026, R&D Systems, 1:500) and secondary (goat α-mouse-AlexaFluor488, 1:500) antibodies. Widefield epifluorescence microscopy was performed on a Motic inverted fluorescence microscope and images were analyzed with Fiji/ImageJ.

For ERGIC-53 and S expression, Vero E6-hAT cells were seeded at 1.5 x 10^5 cells/dish overnight into MatTek dishes, infected with virus (MOI=0.01) for 1 h, washed with PBS, and fed with DMEM-10. After 24 h, cells were fixed and prepared according to the above standard protocol with primary (mouse α-ERGIC-53 C-6, Santa Cruz, 1:100 and rabbit α-S 40150-R007 Sino Biological, 1:500) and secondary (goat α-mouse-AlexFluor488, 1:500 and goat α-rabbit-AlexaFluor568, Invitrogen, 1:500) antibodies. Confocal laser scanning microscopy was performed with a Nikon A1 microscope equipped with a motorized piezo Z stage and images were analyzed with Nikon Elements.

Cell fusion assay

Vero E6-hAT and induced Vero E6-hAT-coE cells were seeded at 1 x 10^6 cells/dish overnight in MatTek dishes, infected with virus (MOI=0.01) for 1 h, washed with PBS, and fed with DMEM-10 supplemented with NAb (1 µg/ml). After 24 h, cells were fixed

and prepared according to the above standard protocol with primary (mouse α-nLuc MAB10026, 1:500) and secondary (goat α-mouse-AlexaFluor647, Invitrogen, 1:500) antibodies. Confocal laser scanning microscopy was performed with a Nikon A1 microscope, with single focal plane images taken of 9-10 fields on average for four independent experiments. Images were analyzed and total area of each syncytium (as indicated by nLuc expression) was determined with Nikon Elements software.

Split-eGFP BiFC syncytia assay

Vero E6-hAT-N and Vero E6-hAT-C cells with and without induced expression of coE were co-cultured 1:1 at 1 x 10^6 total cells/dish overnight in MatTek dishes, infected with virus (MOI=0.01) for 1 h, washed with PBS, and fed with DMEM-10 supplemented with NAb (1 µg/ml). After 24 h, cells were fixed and prepared according to the above standard protocol with primary (mouse α-nLuc MAB10026, 1:500) and secondary (goat α-mouse-AlexFluor647, 1:500) antibodies. Confocal laser scanning microscopy was performed with a Nikon A1 microscope, with single focal plane images taken of 6 fields each for two independent experiments. Images were analyzed with Nikon Elements software.

S localization assay

Vero E6-hAT cells were seeded at 1.5 x 10^5 cells/dish overnight in MatTek dishes, infected with virus (MOI=0.01) for 1 h, washed with PBS, and fed with DMEM-10. After 24 h, cells were fixed with 4% PFA for 24 h at 4° C, blocked with normal goat serum, incubated with primary (rabbit α-S 40150-R007, 1:500), and secondary (goat α-rabbit-AlexaFluor568, 1:500) surface antibodies, permeabilized, re-blocked, incubated with primary (rabbit α-S 40150-R007, 1:500) and secondary (goat α-rabbit-AlexaFluor488, Invitrogen 1:500) surface/intracellular antibodies, and counterstained with Hoechst 33342. Confocal laser scanning microscopy was performed with a Nikon A1 microscope equipped with a motorized piezo Z stage, with 4-6 Z-stacks taken for each of two independent experiments. Images were analyzed with Nikon Elements software.

Statistics

Results were analyzed for statistical significance by two-sided student t test with Prism software (GraphPad). A p-value of less than or equal to 0.05 was used to indicate statistical significance.

Acknowledgements

This work was supported by National Institutes of Health (NIH) grants HL129949 (H.L.F), AI180311 (W.P.D.), AI175795 (Z.A.), and the Pittsburgh CTSI COVID-19 Pilot Program (Z.A.). The Pittsburgh Center for CryoEM (RRID:SCR_025216) used for data collection in this project was supported, in part, by the University of Pittsburgh, the School of Medicine, and the Department of Structural Biology.

References

1. Zhu N, Zhang D, Wang W, Li X, Yang B, Song J, Zhao X, Huang B, Shi W, Lu R, Niu P, Zhan F, Ma X, Wang D, Xu W, Wu G, Gao GF, Tan W, Team CNCI and R. 2020. A Novel Coronavirus from Patients with Pneumonia in China, 2019. N Engl J Med 382:727–733.

2. Rota PA, Oberste MS, Monroe SS, Nix WA, Campagnoli R, Icenogle JP, Peñaranda S, Bankamp B, Maher K, Chen M, Tong S, Tamin A, Lowe L, Frace M, DeRisi JL, Chen Q, Wang D, Erdman DD, Peret TCT, Burns C, Ksiazek TG, Rollin PE, Sanchez A, Liffick S, Holloway B, Limor J, McCaustland K, Olsen-Rasmussen M, Fouchier R, Günther S, Osterhaus ADME, Drosten C, Pallansch MA, Anderson LJ, Bellini WJ. 2003. Characterization of a Novel Coronavirus Associated with Severe Acute Respiratory Syndrome. Science 300:1394–1399.

3. Zaki AM, Boheemen S van, Bestebroer TM, Osterhaus ADME, Fouchier RAM. 2012. Isolation of a Novel Coronavirus from a Man with Pneumonia in Saudi Arabia. New Engl J Medicine 367:1814–1820.

4. Huang C, Wang Y, Li X, Ren L, Zhao J, Hu Y, Zhang L, Fan G, Xu J, Gu X, Cheng Z, Yu T, Xia J, Wei Y, Wu W, Xie X, Yin W, Li H, Liu M, Xiao Y, Gao H, Guo L, Xie J, Wang G, Jiang R, Gao Z, Jin Q, Wang J, Cao B. 2020. Clinical features of patients infected with 2019 novel coronavirus in Wuhan, China. Lancet Lond Engl 395:497–506.

5. Lake MA. 2020. What we know so far: COVID-19 current clinical knowledge and research. Clin Med (Lond) 20:124–127.

6. Chen N, Zhou M, Dong X, Qu J, Gong F, Han Y, Qiu Y, Wang J, Liu Y, Wei Y, Xia J, Yu T, Zhang X, Zhang L. 2020. Epidemiological and clinical characteristics of 99 cases of 2019 novel coronavirus pneumonia in Wuhan, China: a descriptive study. Lancet Lond Engl 395:507–513.

7. Godfred-Cato S, Bryant B, Leung J, Oster ME, Conklin L, Abrams J, Roguski K, Wallace B, Prezzato E, Koumans EH, Lee EH, Geevarughese A, Lash MK, Reilly KH, Pulver WP, Thomas D, Feder KA, Hsu KK, Plipat N, Richardson G, Reid H, Lim S, Schmitz A, Pierce T, Hrapcak S, Datta D, Morris SB, Clarke K, Belay E, Team CM-CR. 2020. COVID-19–Associated Multisystem Inflammatory Syndrome in Children — United States, March–July 2020. Morb Mortal Wkly Rep 69:1074–1080.

8. Becker JH, Lin JJ, Doernberg M, Stone K, Navis A, Festa JR, Wisnivesky JP. 2021. Assessment of Cognitive Function in Patients After COVID-19 Infection. Jama Netw Open 4:e2130645.

9. Groff D, Sun A, Ssentongo AE, Ba DM, Parsons N, Poudel GR, Lekoubou A, Oh JS, Ericson JE, Ssentongo P, Chinchilli VM. 2021. Short-term and Long-term Rates of Postacute Sequelae of SARS-CoV-2 Infection. Jama Netw Open 4:e2128568.

10. Organization WH. WHO Coronavirus (COVID-19) Dashboard > Cases. https://data.who.int/dashboards/covid19/cases. Retrieved 28 February 2025.

11. Organization WH. WHO Coronavirus (COVID-19) Dashboard > Deaths. https://data.who.int/dashboards/covid19/deaths. Retrieved 28 February 2025.

12. Davis HE, McCorkell L, Vogel JM, Topol EJ. 2023. Long COVID: major findings, mechanisms and recommendations. Nat Rev Microbiol 21:133–146.

13. Greenhalgh T, Sivan M, Perlowski A, Nikolich JŽ. 2024. Long COVID: a clinical update. Lancet 404:707–724.

14. Feikin DR, Higdon MM, Abu-Raddad LJ, Andrews N, Araos R, Goldberg Y, Groome MJ, Huppert A, O'Brien KL, Smith PG, Wilder-Smith A, Zeger S, Knoll MD, Patel MK. 2022. Duration of effectiveness of vaccines against SARS-CoV-2 infection and COVID-19 disease: results of a systematic review and meta-regression. Lancet 399:924–944.

15. Pooley N, Karim SSA, Combadière B, Ooi EE, Harris RC, Seblain CEG, Kisomi M, Shaikh N. 2023. Durability of Vaccine-Induced and Natural Immunity Against COVID-19: A Narrative Review. Infect Dis Ther 12:367–387.

16. Ong SWX, Chia T, Young BE. 2022. SARS-CoV-2 variants of concern and vaccine escape, from Alpha to Omicron and beyond. Expert Rev Respir Med 16:499–502.

17. Carabelli AM, Peacock TP, Thorne LG, Harvey WT, Hughes J, Silva TI de, Peacock SJ, Barclay WS, Silva TI de, Towers GJ, Robertson DL. 2023. SARS-CoV-2 variant biology: immune escape, transmission and fitness. Nat Rev Microbiol 21:162–177.

18. Abdoli A, Jamshidi H, Taqavian M, Baghal ML, Jalili H. 2024. Omicron-specific and bivalent omicron-containing vaccine candidates elicit potent virus neutralisation in the animal model. Sci Rep 14:268.

19. Andrews HS, Herman JD, Gandhi RT. 2023. Treatments for COVID-19. Annu Rev Med 75:145–157.

20. Zhou L, Ayeh SK, Chidambaram V, Karakousis PC. 2021. Modes of transmission of SARS-CoV-2 and evidence for preventive behavioral interventions. Bmc Infect Dis 21:496.

21. Rabaan AA, Al-Ahmed SH, Al-Malkey M, Alsubki R, Ezzikouri S, Al-Hababi FH, Sah R, Mutair AA, Alhumaid S, Al-Tawfiq JA, Al-Omari A, Al-Qaaneh AM, Al-Qahtani M, Tirupathi R, Hamad MAA, Al-Baghli NA, Sulaiman T, Alsubait A, Mehta R, Abass E,

Alawi M, Alshahrani F, Shrestha DB, Karobari MI, Pecho-Silva S, Arteaga-Livias K, Bonilla-Aldana DK, Rodriguez-Morales AJ. 2021. Airborne transmission of SARS-CoV-2 is the dominant route of transmission: droplets and aerosols. Le Infez Med 29:10–19.

22. Sungnak W, Huang N, Bécavin C, Berg M, Queen R, Litvinukova M, Talavera-López C, Maatz H, Reichart D, Sampaziotis F, Worlock KB, Yoshida M, Barnes JL, Banovich NE, Barbry P, Brazma A, Collin J, Desai TJ, Duong TE, Eickelberg O, Falk C, Farzan M, Glass I, Gupta RK, Haniffa M, Horvath P, Hubner N, Hung D, Kaminski N, Krasnow M, Kropski JA, Kuhnemund M, Lako M, Lee H, Leroy S, Linnarson S, Lundeberg J, Meyer KB, Miao Z, Misharin AV, Nawijn MC, Nikolic MZ, Noseda M, Ordovas-Montanes J, Oudit GY, Pe'er D, Powell J, Quake S, Rajagopal J, Tata PR, Rawlins EL, Regev A, Reyfman PA, Rozenblatt-Rosen O, Saeb-Parsy K, Samakovlis C, Schiller HB, Schultze JL, Seibold MA, Seidman CE, Seidman JG, Shalek AK, Shepherd D, Spence J, Spira A, Sun X, Teichmann SA, Theis FJ, Tsankov AM, Vallier L, Berge M van den, Whitsett J, Xavier R, Xu Y, Zaragosi L-E, Zerti D, Zhang H, Zhang K, Rojas M, Figueiredo F. 2020. SARS-CoV-2 entry factors are highly expressed in nasal epithelial cells together with innate immune genes. Nat Med 26:681–687.

23. Hou YJ, Okuda K, Edwards CE, Martinez DR, Asakura T, Dinnon KH, Kato T, Lee RE, Yount BL, Mascenik TM, Chen G, Olivier KN, Ghio A, Tse LV, Leist SR, Gralinski LE, Schäfer A, Dang H, Gilmore R, Nakano S, Sun L, Fulcher ML, Livraghi-Butrico A, Nicely NI, Cameron M, Cameron C, Kelvin DJ, Silva A de, Margolis DM, Markmann A, Bartelt L, Zumwalt R, Martinez FJ, Salvatore SP, Borczuk A, Tata PR, Sontake V, Kimple A, Jaspers I, O'Neal WK, Randell SH, Boucher RC, Baric RS. 2020. SARS-CoV-2 Reverse Genetics Reveals a Variable Infection Gradient in the Respiratory Tract. Cell 182:429-446.e14.

24. Lamers MM, Beumer J, Vaart J van der, Knoops K, Puschhof J, Breugem TI, Ravelli RBG, Schayck JP van, Mykytyn AZ, Duimel HQ, Donselaar E van, Riesebosch S, Kuijpers HJH, Schipper D, Wetering WJ van de, Graaf M de, Koopmans M, Cuppen E, Peters PJ, Haagmans BL, Clevers H. 2020. SARS-CoV-2 productively infects human gut enterocytes. Science 369:50–54.

25. Jackson CB, Farzan M, Chen B, Choe H. 2022. Mechanisms of SARS-CoV-2 entry into cells. Nat Rev Mol Cell Biol 23:3–20.

26. Hoffmann M, Kleine-Weber H, Pöhlmann S. 2020. A Multibasic Cleavage Site in the Spike Protein of SARS-CoV-2 Is Essential for Infection of Human Lung Cells. Mol Cell 78:779-784.e5.

27. Hoffmann M, Kleine-Weber H, Schroeder S, Krüger N, Herrler T, Erichsen S, Schiergens TS, Herrler G, Wu N-H, Nitsche A, Müller MA, Drosten C, Pöhlmann S. 2020. SARS-CoV-2 Cell Entry Depends on ACE2 and TMPRSS2 and Is Blocked by a Clinically Proven Protease Inhibitor. Cell https://doi.org/10.1016/j.cell.2020.02.052.

28. Matsuyama S, Nao N, Shirato K, Kawase M, Saito S, Takayama I, Nagata N, Sekizuka T, Katoh H, Kato F, Sakata M, Tahara M, Kutsuna S, Ohmagari N, Kuroda M, Suzuki T, Kageyama T, Takeda M. 2020. Enhanced isolation of SARS-CoV-2 by TMPRSS2-expressing cells. Proc Natl Acad Sci 117:7001–7003.

29. V'kovski P, Kratzel A, Steiner S, Stalder H, Thiel V. 2021. Coronavirus biology and replication: implications for SARS-CoV-2. Nat Rev Microbiol 19:155–170.

30. Malone B, Urakova N, Snijder EJ, Campbell EA. 2022. Structures and functions of coronavirus replication–transcription complexes and their relevance for SARS-CoV-2 drug design. Nat Rev Mol Cell Biol 23:21–39.

31. Breitinger U, Farag NS, Sticht H, Breitinger H-G. 2022. Viroporins: Structure, function, and their role in the life cycle of SARS-CoV-2. Int J Biochem Cell Biol 145:106185.

32. Mandala VS, McKay MJ, Shcherbakov AA, Dregni AJ, Kolocouris A, Hong M. 2020. Structure and drug binding of the SARS-CoV-2 envelope protein transmembrane domain in lipid bilayers. Nat Struct Mol Biol 27:1202–1208.

33. Arya R, Kumari S, Pandey B, Mistry H, Bihani SC, Das A, Prashar V, Gupta GD, Panicker L, Kumar M. 2021. Structural insights into SARS-CoV-2 proteins. J Mol Biol 433:166725.

34. Caillet-Saguy C, Durbesson F, Rezelj VV, Gogl G, Tran QD, Twizere J, Vignuzzi M, Vincentelli R, Wolff N. 2021. Host PDZ-containing proteins targeted by SARS-CoV-2. FEBS J 288:5148–5162.

35. Nieto-Torres JL, DeDiego ML, Álvarez E, Jiménez-Guardeño JM, Regla-Nava JA, Llorente M, Kremer L, Shuo S, Enjuanes L. 2011. Subcellular location and topology of severe acute respiratory syndrome coronavirus envelope protein. Virology 415:69–82.

36. Schoeman D, Fielding BC. 2019. Coronavirus envelope protein: current knowledge. Virol J 16:69.

37. Bracquemond D, Muriaux D. 2021. Betacoronavirus Assembly: Clues and Perspectives for Elucidating SARS-CoV-2 Particle Formation and Egress. Mbio 12:e02371-21.

38. Boson B, Legros V, Zhou B, Siret E, Mathieu C, Cosset F-L, Lavillette D, Denolly S. 2021. The SARS-CoV-2 envelope and membrane proteins modulate maturation and retention of the spike protein, allowing assembly of virus-like particles. J Biol Chem 296:100111.

39. Jimenez-Guardeño JM, Nieto-Torres JL, DeDiego ML, Regla-Nava JA, Fernandez-Delgado R, Castaño-Rodriguez C, Enjuanes L. 2014. The PDZ-Binding Motif of Severe

Acute Respiratory Syndrome Coronavirus Envelope Protein Is a Determinant of Viral Pathogenesis. PLoS Pathog 10:e1004320.

40. DeDiego ML, Nieto-Torres JL, Jimenez-Guardeño JM, Regla-Nava JA, Castaño-Rodriguez C, Fernandez-Delgado R, Usera F, Enjuanes L. 2014. Coronavirus virulence genes with main focus on SARS-CoV envelope gene. Virus Res 194:124–137.

41. Ortego J, Ceriani JE, Patiño C, Plana J, Enjuanes L. 2007. Absence of E protein arrests transmissible gastroenteritis coronavirus maturation in the secretory pathway. Virology 368:296–308.

42. Stodola JK, Dubois G, Coupanec AL, Desforges M, Talbot PJ. 2018. The OC43 human coronavirus envelope protein is critical for infectious virus production and propagation in neuronal cells and is a determinant of neurovirulence and CNS pathology. Virology 515:134–149.

43. Almazán F, DeDiego ML, Sola I, Zuñiga S, Nieto-Torres JL, Marquez-Jurado S, Andrés G, Enjuanes L. 2013. Engineering a replication-competent, propagation-defective Middle East respiratory syndrome coronavirus as a vaccine candidate. mBio 4:e00650-13.

44. Kuo L, Masters PS. 2003. The Small Envelope Protein E Is Not Essential for Murine Coronavirus Replication. J Virol 77:4597–4608.

45. DeDiego ML, Álvarez E, Almazán F, Rejas MT, Lamirande E, Roberts A, Shieh W-J, Zaki SR, Subbarao K, Enjuanes L. 2007. A severe acute respiratory syndrome coronavirus that lacks the E gene is attenuated in vitro and in vivo. J Virol 81:1701–1713.

46. Castaño-Rodriguez C, Honrubia JM, Gutiérrez-Álvarez J, DeDiego ML, Nieto-Torres JL, Jimenez-Guardeño JM, Regla-Nava JA, Fernandez-Delgado R, Verdia-Báguena C, Queralt-Martín M, Kochan G, Perlman S, Aguilella VM, Sola I, Enjuanes L. 2018. Role of Severe Acute Respiratory Syndrome Coronavirus Viroporins E, 3a, and 8a in Replication and Pathogenesis. mBio 9:10.1128/mbio.02325-17.

47. Zhang X, Liu Y, Liu J, Bailey AL, Plante KS, Plante JA, Zou J, Xia H, Bopp NE, Aguilar PV, Ren P, Menachery VD, Diamond MS, Weaver SC, Xie X, Shi P-Y. 2021. A trans-complementation system for SARS-CoV-2 recapitulates authentic viral replication without virulence. Cell 184:2229-2238.e13.

48. Almazán F, DeDiego ML, Galán C, Escors D, Álvarez E, Ortego J, Sola I, Zuñiga S, Alonso S, Moreno JL, Nogales A, Capiscol C, Enjuanes L. 2006. Construction of a severe acute respiratory syndrome coronavirus infectious cDNA clone and a replicon to study coronavirus RNA synthesis. J Virol 80:10900–10906.

49. Wild J, Hradecna Z, Szybalski W. 2002. Conditionally Amplifiable BACs: Switching From Single-Copy to High-Copy Vectors and Genomic Clones. Genome Res 12:1434–1444.

50. Buchrieser J, Dufloo J, Hubert M, Monel B, Planas D, Rajah MM, Planchais C, Porrot F, Guivel-Benhassine F, Werf SV der, Casartelli N, Mouquet H, Bruel T, Schwartz O. 2020. Syncytia formation by SARS-CoV-2-infected cells. EMBO J 39:EMBJ2020106267.

51. Zeng C, Evans JP, King T, Zheng Y-M, Oltz EM, Whelan SPJ, Saif LJ, Peeples ME, Liu S-L. 2022. SARS-CoV-2 spreads through cell-to-cell transmission. Proc National Acad Sci 119:e2111400119.

52. Marovich M, Mascola JR, Cohen MS. 2020. Monoclonal Antibodies for Prevention and Treatment of COVID-19. JAMA 324:131–132.

53. Taylor PC, Adams AC, Hufford MM, Torre I de la, Winthrop K, Gottlieb RL. 2021. Neutralizing monoclonal antibodies for treatment of COVID-19. Nat Rev Immunol 21:382–393.

54. Brimacombe CL, Grove J, Meredith LW, Hu K, Syder AJ, Flores MV, Timpe JM, Krieger SE, Baumert TF, Tellinghuisen TL, Wong-Staal F, Balfe P, McKeating JA. 2010. Neutralizing Antibody-Resistant Hepatitis C Virus Cell-to-Cell Transmission. J Virol 85:596–605.

55. Miao C, Li M, Zheng Y-M, Cohen FS, Liu S-L. 2016. Cell–cell contact promotes Ebola virus GP-mediated infection. Virology 488:202–215.

56. Li H, Zony C, Chen P, Chen BK. 2017. Reduced Potency and Incomplete Neutralization of Broadly Neutralizing Antibodies against Cell-to-Cell Transmission of HIV-1 with Transmitted Founder Envs. J Virol 91:10.1128/jvi.02425-16.

57. Jones BE, Brown-Augsburger PL, Corbett KS, Westendorf K, Davies J, Cujec TP, Wiethoff CM, Blackbourne JL, Heinz BA, Foster D, Higgs RE, Balasubramaniam D, Wang L, Zhang Y, Yang ES, Bidshahri R, Kraft L, Hwang Y, Žentelis S, Jepson KR, Goya R, Smith MA, Collins DW, Hinshaw SJ, Tycho SA, Pellacani D, Xiang P, Muthuraman K, Sobhanifar S, Piper MH, Triana FJ, Hendle J, Pustilnik A, Adams AC, Berens SJ, Baric RS, Martinez DR, Cross RW, Geisbert TW, Borisevich V, Abiona O, Belli HM, Vries M de, Mohamed A, Dittmann M, Samanovic MI, Mulligan MJ, Goldsmith JA, Hsieh C-L, Johnson NV, Wrapp D, McLellan JS, Barnhart BC, Graham BS, Mascola JR, Hansen CL, Falconer E. 2021. The neutralizing antibody, LY-CoV555, protects against SARS-CoV-2 infection in nonhuman primates. Sci Transl Med 13:eabf1906.

58. Nathan R, Shawa I, Torre IDL, Pustizzi JM, Haustrup N, Patel DR, Huhn G. 2021. A Narrative Review of the Clinical Practicalities of Bamlanivimab and Etesevimab Antibody Therapies for SARS-CoV-2. Infect Dis Ther 10:1933–1947.

59. VanBlargan LA, Errico JM, Halfmann PJ, Zost SJ, Crowe JE, Purcell LA, Kawaoka Y, Corti D, Fremont DH, Diamond MS. 2022. An infectious SARS-CoV-2 B.1.1.529 Omicron virus escapes neutralization by therapeutic monoclonal antibodies. Nat Med 28:490–495.

60. Nambulli S, Rennick LJ, Acciardo AS, Tilston-Lunel NL, Ho G, Crossland NA, Hardcastle K, Nieto B, Bainbridge G, Williams T, Sharp CR, Duprex WP. 2022. FeMV is a cathepsin-dependent unique morbillivirus infecting the kidneys of domestic cats. Proc Natl Acad Sci 119:e2209405119.

61. Cattin-Ortolá J, Welch LG, Maslen SL, Papa G, James LC, Munro S. 2021. Sequences in the cytoplasmic tail of SARS-CoV-2 Spike facilitate expression at the cell surface and syncytia formation. Nat Commun 12:5333.

62. Finkel Y, Gluck A, Nachshon A, Winkler R, Fisher T, Rozman B, Mizrahi O, Lubelsky Y, Zuckerman B, Slobodin B, Yahalom-Ronen Y, Tamir H, Ulitsky I, Israely T, Paran N, Schwartz M, Stern-Ginossar N. 2021. SARS-CoV-2 uses a multipronged strategy to impede host protein synthesis. Nature 594:240–245.

63. Thoms M, Buschauer R, Ameismeier M, Koepke L, Denk T, Hirschenberger M, Kratzat H, Hayn M, Mackens-Kiani T, Cheng J, Straub JH, Stürzel CM, Fröhlich T, Berninghausen O, Becker T, Kirchhoff F, Sparrer KMJ, Beckmann R. 2020. Structural basis for translational shutdown and immune evasion by the Nsp1 protein of SARS-CoV-2. Science 369:1249–1255.

64. Zhang K, Miorin L, Makio T, Dehghan I, Gao S, Xie Y, Zhong H, Esparza M, Kehrer T, Kumar A, Hobman TC, Ptak C, Gao B, Minna JD, Chen Z, García-Sastre A, Ren Y, Wozniak RW, Fontoura BMA. 2021. Nsp1 protein of SARS-CoV-2 disrupts the mRNA export machinery to inhibit host gene expression. Sci Adv 7:eabe7386.

65. Miura K, Suzuki Y, Ishida K, Arakawa M, Wu H, Fujioka Y, Emi A, Maeda K, Hamajima R, Nakano T, Tenno T, Hiroaki H, Morita E. 2023. Distinct motifs in the E protein are required for SARS-CoV-2 virus particle formation and lysosomal deacidification in host cells. J Virol 97:e00426-23.

66. Kuo L, Hurst KR, Masters PS. 2006. Exceptional Flexibility in the Sequence Requirements for Coronavirus Small Envelope Protein Function. J Virol 81:2249–2262.

67. Shepley-McTaggart A, Sagum CA, Oliva I, Rybakovsky E, DiGuilio K, Liang J, Bedford MT, Cassel J, Sudol M, Mullin JM, Harty RN. 2021. SARS-CoV-2 Envelope (E) protein interacts with PDZ-domain-2 of host tight junction protein ZO1. Plos One 16:e0251955.

68. Zhu Y, Alvarez F, Wolff N, Mechaly A, Brûlé S, Neitthoffer B, Etienne-Manneville S, Haouz A, Boëda B, Caillet-Saguy C. 2022. Interactions of Severe Acute Respiratory

Syndrome Coronavirus 2 Protein E With Cell Junctions and Polarity PSD-95/Dlg/ZO-1-Containing Proteins. Front Microbiol 13:829094.

69. Xu J-B, Guan W-J, Zhang Y-L, Qiu Z-E, Chen L, Hou X-C, Yue J, Zhou Y-Y, Sheng J, Zhao L, Zhu Y-X, Sun J, Zhao J, Zhou W-L, Zhong N-S. 2024. SARS-CoV-2 envelope protein impairs airway epithelial barrier function and exacerbates airway inflammation via increased intracellular Cl− concentration. Signal Transduct Target Ther 9:74.

70. Berta B, Tordai H, Lukács GL, Papp B, Enyedi Á, Padányi R, Hegedűs T. 2024. SARS-CoV-2 envelope protein alters calcium signaling via SERCA interactions. Sci Rep 14:21200.

71. Braga L, Ali H, Secco I, Chiavacci E, Neves G, Goldhill D, Penn R, Jimenez-Guardeño JM, Ortega-Prieto AM, Bussani R, Cannatà A, Rizzari G, Collesi C, Schneider E, Arosio D, Shah AM, Barclay WS, Malim MH, Burrone J, Giacca M. 2021. Drugs that inhibit TMEM16 proteins block SARS-CoV-2 spike-induced syncytia. Nature 594:88–93.

72. Rajah MM, Bernier A, Buchrieser J, Schwartz O. 2022. The Mechanism and Consequences of SARS-CoV-2 Spike-Mediated Fusion and Syncytia Formation. J Mol Biol 434:167280.

73. Saraste J, Prydz K. 2021. Assembly and Cellular Exit of Coronaviruses: Hijacking an Unconventional Secretory Pathway from the Pre-Golgi Intermediate Compartment via the Golgi Ribbon to the Extracellular Space. Cells 10:503.

74. Saraste J, Enyioko M, Dale H, Prydz K, Machamer C. 2022. Evidence for the role of Rab11-positive recycling endosomes as intermediates in coronavirus egress from epithelial cells. Histochem Cell Biol 158:241–251.

75. Ghosh S, Dellibovi-Ragheb TA, Kerviel A, Pak E, Qiu Q, Fisher M, Takvorian PM, Bleck C, Hsu VW, Fehr AR, Perlman S, Achar SR, Straus MR, Whittaker GR, Haan CAM de, Kehrl J, Altan-Bonnet G, Altan-Bonnet N. 2020. β-Coronaviruses Use Lysosomes for Egress Instead of the Biosynthetic Secretory Pathway. Cell 183:1520-1535.e14.

76. Sergio MC, Ricciardi S, Guarino AM, Giaquinto L, Matteis MAD. 2024. Membrane remodeling and trafficking piloted by SARS-CoV-2. Trends Cell Biol 34:785–800.

77. LAVI E, WANG Q, WEISS SR, GONATAS NK. 1996. Syncytia Formation Induced by Coronavirus Infection Is Associated with Fragmentation and Rearrangement of the Golgi Apparatus. Virology 221:325–334.

78. Scherer KM, Mascheroni L, Carnell GW, Wunderlich LCS, Makarchuk S, Brockhoff M, Mela I, Fernandez-Villegas A, Barysevich M, Stewart H, Sans MS, George CL, Lamb

JR, Kaminski-Schierle GS, Heeney JL, Kaminski CF. 2022. SARS-CoV-2 nucleocapsid protein adheres to replication organelles before viral assembly at the Golgi/ERGIC and lysosome-mediated egress. Sci Adv 8:eabl4895.

79. Hayn M, Hirschenberger M, Koepke L, Nchioua R, Straub JH, Klute S, Hunszinger V, Zech F, Bozzo CP, Aftab W, Christensen MH, Conzelmann C, Müller JA, Badarinarayan SS, Stürzel CM, Forne I, Stenger S, Conzelmann K-K, Münch J, Schmidt FI, Sauter D, Imhof A, Kirchhoff F, Sparrer KMJ. 2021. Systematic functional analysis of SARS-CoV-2 proteins uncovers viral innate immune antagonists and remaining vulnerabilities. Cell Rep 35:109126.

80. Shariq M, Malik AA, Sheikh JA, Hasnain SE, Ehtesham NZ. 2023. Regulation of autophagy by SARS-CoV-2: The multifunctional contributions of ORF3a. J Méd Virol 95:e28959.

81. Yuan Z, Hu B, Xiao H, Tan X, Li Y, Tang K, Zhang Y, Cai K, Ding B. 2022. The E3 Ubiquitin Ligase RNF5 Facilitates SARS-CoV-2 Membrane Protein-Mediated Virion Release. Mbio 13:e03168-21.

82. Nal B, Chan C, Kien F, Siu L, Tse J, Chu K, Kam J, Staropoli I, Crescenzo-Chaigne B, Escriou N, Werf S van der, Yuen K-Y, Altmeyer R. 2005. Differential maturation and subcellular localization of severe acute respiratory syndrome coronavirus surface proteins S, M and E. J Gen Virol 86:1423–1434.

83. Ge L, Melville D, Zhang M, Schekman R. 2013. The ER–Golgi intermediate compartment is a key membrane source for the LC3 lipidation step of autophagosome biogenesis. eLife 2:e00947.

84. Xie X, Muruato A, Lokugamage KG, Narayanan K, Zhang X, Zou J, Liu J, Schindewolf C, Bopp NE, Aguilar PV, Plante KS, Weaver SC, Makino S, LeDuc JW, Menachery VD, Shi P-Y. 2020. An Infectious cDNA Clone of SARS-CoV-2. Cell Host Microbe 27:841-848.e3.

85. Roy CN, Moreno MAB, Kline C, Ambrose Z. 2021. CG Dinucleotide Removal in Bioluminescent and Fluorescent Reporters Improves HIV-1 Replication and Reporter Gene Expression for Dual Imaging in Humanized Mice. J Virol 95:10.1128/jvi.00449-21.

86. Zerbato JM, Khoury G, Zhao W, Gartner MJ, Pascoe RD, Rhodes A, Dantanarayana A, Gooey M, Anderson J, Bacchetti P, Deeks SG, McMahon J, Roche M, Rasmussen TA, Purcell DF, Lewin SR. 2021. Multiply spliced HIV RNA is a predictive measure of virus production ex vivo and in vivo following reversal of HIV latency. EBioMedicine 65:103241.

87. Schindelin J, Arganda-Carreras I, Frise E, Kaynig V, Longair M, Pietzsch T, Preibisch S, Rueden C, Saalfeld S, Schmid B, Tinevez J-Y, White DJ, Hartenstein V,

Eliceiri K, Tomancak P, Cardona A. 2012. Fiji: an open-source platform for biological-image analysis. Nat Methods 9:676–682.

88. Simmons HC, Watanabe A, III THO, Itallie ESV, Wiehe KJ, Sempowski GD, Kuraoka M, Kelsoe G, McCarthy KR. 2023. A new class of antibodies that overcomes a steric barrier to cross-group neutralization of influenza viruses. PLOS Biol 21:e3002415.

Table 1. Primers used for SARS-CoV-2 RT-PCR detection and quantitative RT-PCR (qRT-PCR)

Gene	Use	Forward primer (5' -> 3')	Reverse primer (5' -> 3')	Probe (5'-FAM -> 3'-BHQ1)
ORF1a	gRNA gel	GGCCAATTCTGCTGTCAAATTA	CAGTGCAAGCAGTTTGTGTAG	
S	sgRNA gel	CCAACCAACTTTCGATCTC	TGATTCTCTTCCTGTTCC	
ORF3a	sgRNA gel	CCAACCAACTTTCGATCTC	CTTTTACTCCAGATTCCC	
E	sgRNA gel	CCAACCAACTTTCGATCTC	GAAGGTTTTACAAGACTCACG	
M	sgRNA gel	CCAACCAACTTTCGATCTC	CGGTGATCCAATTTATTCTG	
ORF6	sgRNA gel	CCAACCAACTTTCGATCTC	TCTCCATTGGTTGCTCTTC	
nanoLuc	sgRNA gel	CCAACCAACTTTCGATCTC	AACCCCATCAATTACCAG	
ORF8	sgRNA gel	CCAACCAACTTTCGATCTC	CGCACTACAAGACTACCCA	
N	sgRNA gel	CCAACCAACTTTCGATCTC	GAGGAAGTTGTAGCACGA	
ORF1a	qRT-PCR	GGCCAATTCTGCTGTCAAATTA	CAGTGCAAGCAGTTTGTGTAG	ACAGATGTCTTGTGCTGCCGGTA
E	qRT-PCR	ACAGGTACGTTAATAGTTAATAGCGT	ATATTGCAGCAGTACGCACACA	ACACTAGCCATCCTTACTGCGCTTCG
coE	qRT-PCR	GGCACACTGATCGTTAATAGCG	TTGCAGCAGTAGGCACAC	TGGCTATCCTGACCGCCCTGAG

Figure legends

Figure 1. SARS-CoV-2 BAC system produces infectious virus particles. (A) Vero E6 -hAT cells were infected with WT SARS-CoV-2-nLuc virus (MOI=1) or mock infected for 24 h and imaged by phase contrast microscopy. (B) Plaque titer of WT SARS-CoV-2-nLuc virus on Vero E6-hAT cells. (C,D) RNA was isolated from WT SARS-CoV-2-nLuc virus producer cells (C) and supernatant (D) and ORF1a copies were quantified by qRT-PCR. The dotted line represents the assay limit of detection. Error bars represent standard error of the mean (SEM) for two independent experiments. (E) E6-hAT cells were infected with WT SARS-CoV-2-nLuc virus or mock infected for 48 h and lysates were measured for nLuc activity. Error bars represent SEM for three independent experiments. (F) RNA was isolated from Vero E6-hAT cells infected with WT SARS-CoV-2-nLuc virus and RT-PCR amplified with SARS-CoV-2 sgRNA specific primers and run on an agarose gel. L = 100 bp ladder. (G) Negative stain EM (left) and cryo-EM (right) of WT SARS-CoV-2-nLuc virus particles. Solid white bar represents 50 nm.

Figure 2. ΔE SARS-CoV-2 is replication-competent but attenuated compared to WT virus. (A-C) WT and ΔE SARS-CoV-2-nLuc viruses were serially passaged three times in Vero E6-hAT cells (WT and ΔE) or E6-hAT cells stably expressing coE *in trans* (ΔE only). Dotted lines represent the assay limits of detection. **** $p < 0.0001$, ns $p > 0.05$. Error bars represent SEM for three independent experiments. Plaque titers (A), genomic RNA (ORF1a) copies (B), and infectivity on fresh Vero E6-hAT cells after 72 h (C) were measured for each passage. (D) Indicated cell lines were infected with WT or ΔE SARS-CoV-2 and assayed for nLuc activity after 72 h. Dotted lines represent the assay limits of detection. ** $p < 0.01$, * $p < 0.05$. Error bars represent SEM for 2-3 independent experiments. (E) Representative images of indicated cell lines that were fixed, stained for ACE2 cell surface expression (green) and nuclei (Hoechst; blue), and imaged by confocal microscopy.

Figure 3. ΔE SARS-CoV-2 virus replication produces the expected sgRNAs and does not recombine with trans-complemented coE. (A) RNA was isolated from Vero E6-hAT

(WT and ΔE) or E6-hAT cells stably expressing coE (ΔE only) infected with WT or ΔE SARS-CoV-2-nLuc virus. RT-PCR was performed with SARS-CoV-2 sgRNA specific primers and products were run on an agarose gel. L = 100 bp ladder. (B,C) RNA quantitation of endogenous E (B) or trans-complemented coE (C) copies were measured by qRT-PCR in producer cells (left) and virus (right) from serial passages of WT and ΔE SARS-CoV-2-nLuc shown in **Figure 2**. Dotted lines represent the assay limits of detection. Error bars represent SEM for three independent experiments.

Figure 4. ΔE SARS-CoV-2 is defective for virus particle production and spread and is partially rescued by E trans-complementation. (A) Plaque assays are shown for WT SARS-CoV-2-nLuc infection of Vero E6-hAT cells and ΔE SARS-CoV-2-nLuc infection of Vero E6-hAT cells with or without stable expression of E. Numbers represent log dilution of virus. (B) Negative stain EM (top) and cryo-EM (bottom) of WT and ΔE SARS-CoV-2-nLuc produced with and without trans-complementation of E. Representative micrographs of two independent experiments are shown. Solid white bars represent 50 nm. (C) Immunoblot of S on purified WT and ΔE SARS-CoV-2-nLuc virions, normalized to N expression. (D, E) Vero E6-hAT cells with or without stable expression of E were infected with WT or ΔE SARS-CoV-2-nLuc for 24 h, stained for nLuc, and imaged by widefield epifluorescence microscopy. Representative micrographs of three independent experiments are shown.

Figure 5. S NAb inhibits SARS-CoV-2 virus particle spread but not cell-to-cell transmission**.** (A) Vero E6-hAT cells were inoculated with WT or ΔE SARS-CoV-2-nLuc virus, which was pretreated with NAb for 1h, and assayed for nLuc activity after 24 h. Results for each virus are normalized to the no NAb condition. Error bars represent SEM for two independent experiments. (B,C) Vero E6-hAT cells were inoculated with WT or ΔE SARS-CoV-2-nLuc virus for 1h, treated with NAb, and after 24 h (B) assayed for nLuc activity or (C) antibody stained for nLuc and imaged by widefield epifluorescence microscopy. Results for each virus are normalized to the no NAb condition. Error bars represent SEM for 3 independent experiments. Representative micrographs of two independent experiments are shown.

Figure 6. SARS-CoV-2-mediated cell fusion is enhanced by E expression in infected target cells. (A,B) Vero E6-hAT cells with and without stable E expression were infected with WT or ∆E SARS-CoV-2-nLuc virus (MOI=0.01) for 1 h, treated with Nab for 24 h, and stained with Hoechst (blue) and nLuc (red). mRuby3 expression was also assessed (white). Representative confocal micrographs (A) and quantification of 35-40 total fields per condition (B) are shown. Solid white bars represent 50 µm. **** $p < 0.0001$, *** $p < 0.001$, ** $p < 0.01$, * $p < 0.05$, ns $p > 0.05$. Error bars represent SEM for four independent experiments.

Figure 7. Lack of E during SARS-CoV-2 infection results in greater S cell surface expression. (A,B) Vero E6-hAT cells were infected with WT or ∆E SARS-CoV-2-nLuc virus for 24 h and stained for surface (red) and internal (green) S expression and Hoechst (blue). Representative confocal micrographs (A) in volume (top) and maximum intensity (bottom) projections are shown. Quantification of internal and external S was performed and graphed as a ratio (B). Error bars represent SEM for two independent experiments.

Figure 8. Lack of E during SARS-CoV-2 infection results in ERGIC reorganization. (A,B) Vero E6-hAT cells were infected with WT or ∆E SARS-CoV-2-nLuc for 24 h, stained for ERGIC-53 (green), S (red) and Hoechst (blue), and imaged by confocal microscopy.

Figure 9. Model schematic comparing WT and ∆E SARS-CoV-2 replication.

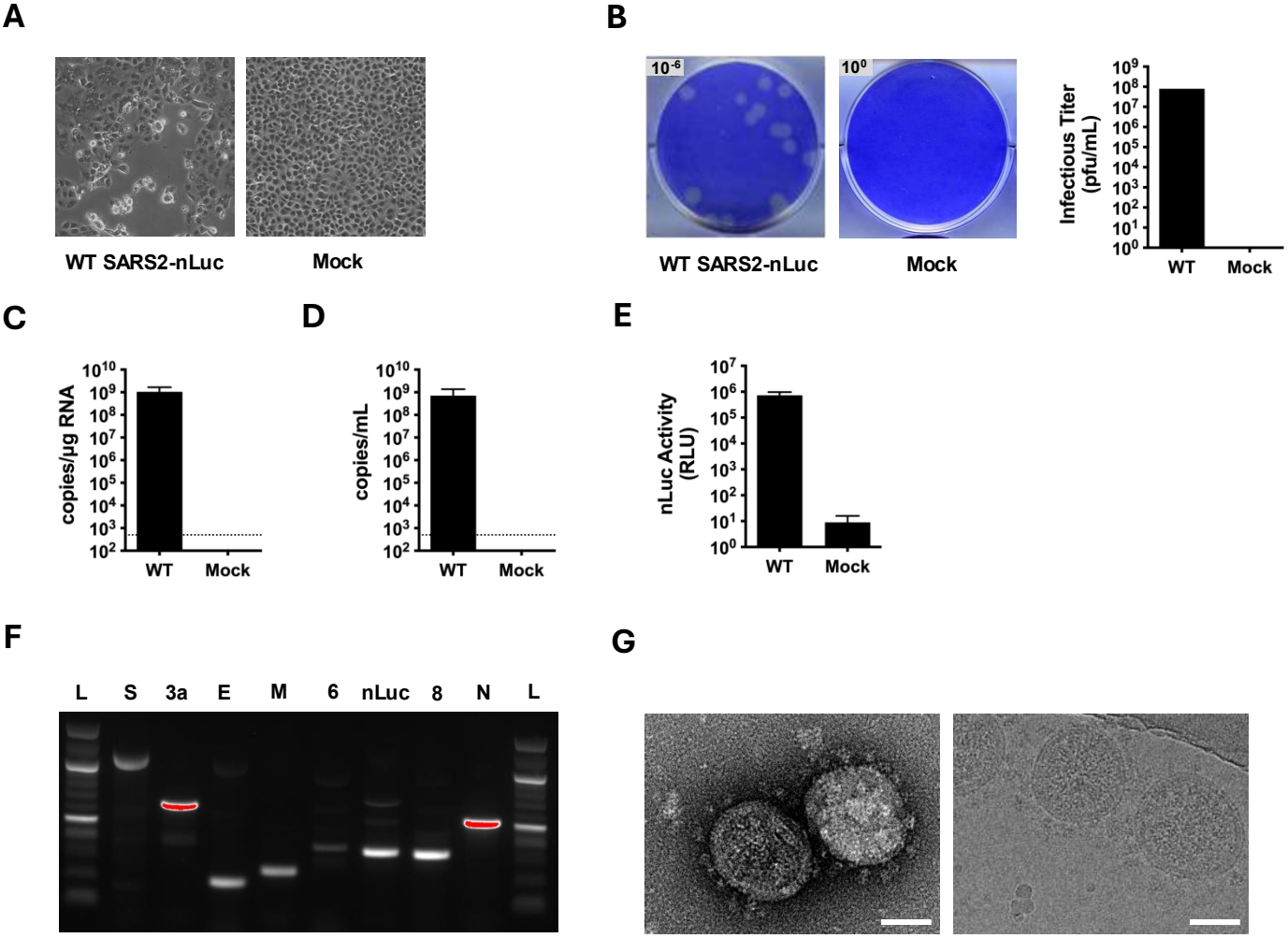
A
WT SARS2-nLuc
Mock
B
10^{-6}
10^{0}
WT SARS2-nLuc
Mock
Infectious Titer (pfu/mL)
WT
Mock
C
copies/µg RNA
WT
Mock
D
copies/mL
WT
Mock
E
nLuc Activity (RLU)
WT
Mock
F
L S 3a E M 6 nLuc 8 N L
G

Figure 1

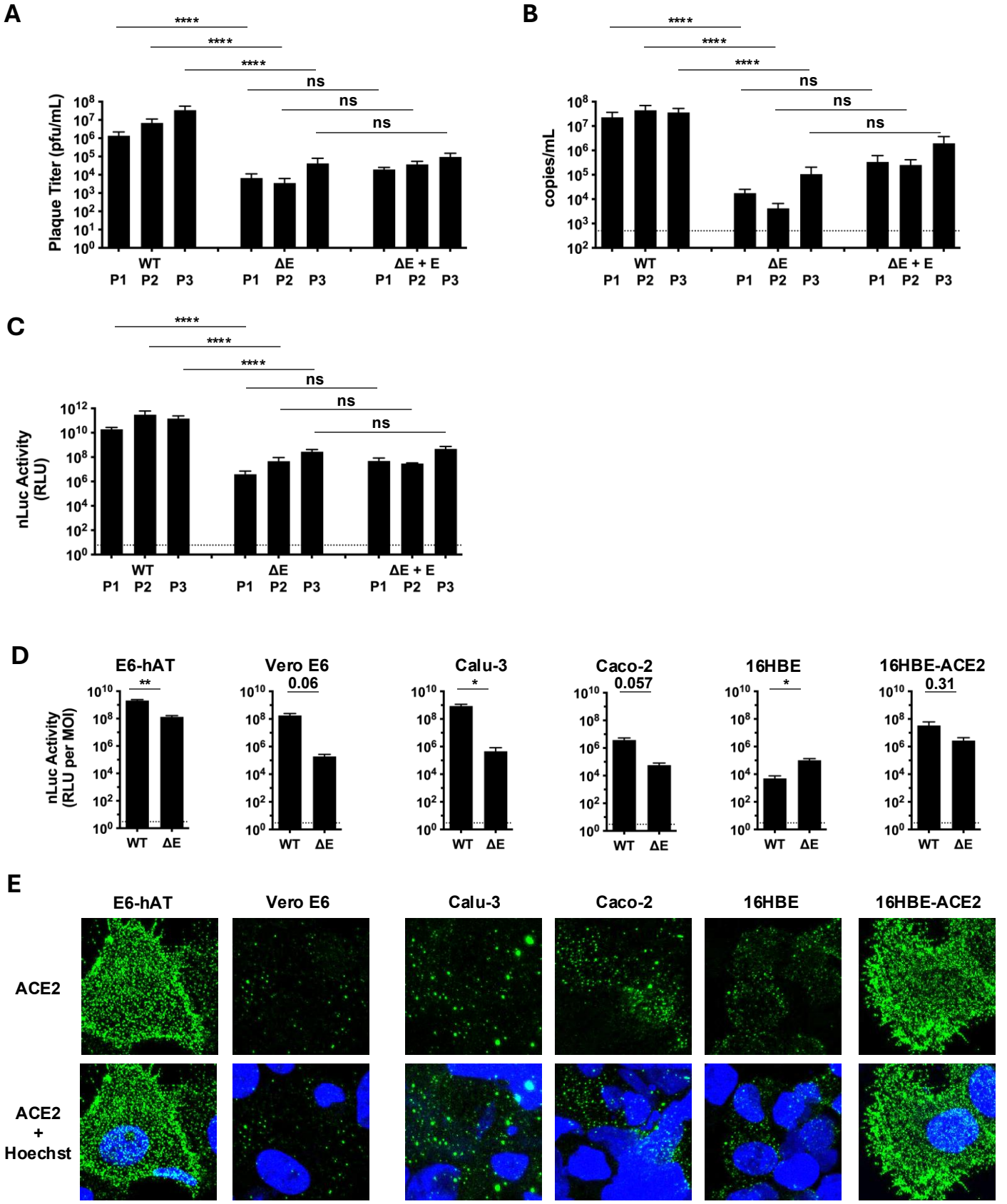
A
Plaque Titer (pfu/mL)
****
****
****
ns
ns
ns
WT
ΔE
ΔE + E
P1 P2 P3
B
copies/mL
C
nLuc Activity (RLU)
D
nLuc Activity (RLU per MOI)
E6-hAT
Vero E6
Calu-3
Caco-2
16HBE
16HBE-ACE2
**
0.06
*
0.057
*
0.31
E
ACE2
ACE2 + Hoechst

Figure 2

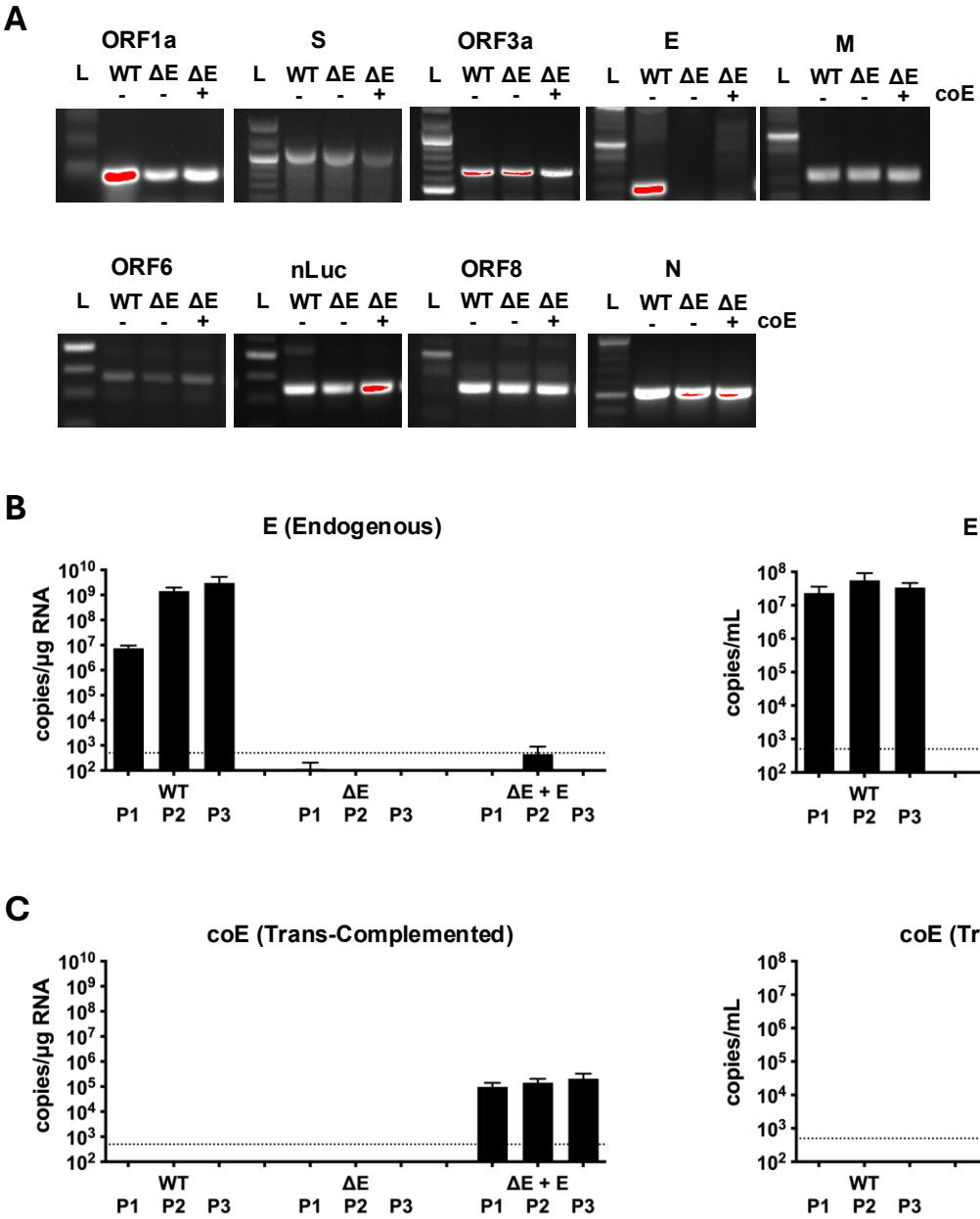
A
ORF1a
S
ORF3a
E
M
ORF6
nLuc
ORF8
N
L WT ΔE ΔE
- - +
coE
B
E (Endogenous)
copies/µg RNA
copies/mL
WT
ΔE
ΔE + E
P1 P2 P3
C
coE (Trans-Complemented)

Figure 3

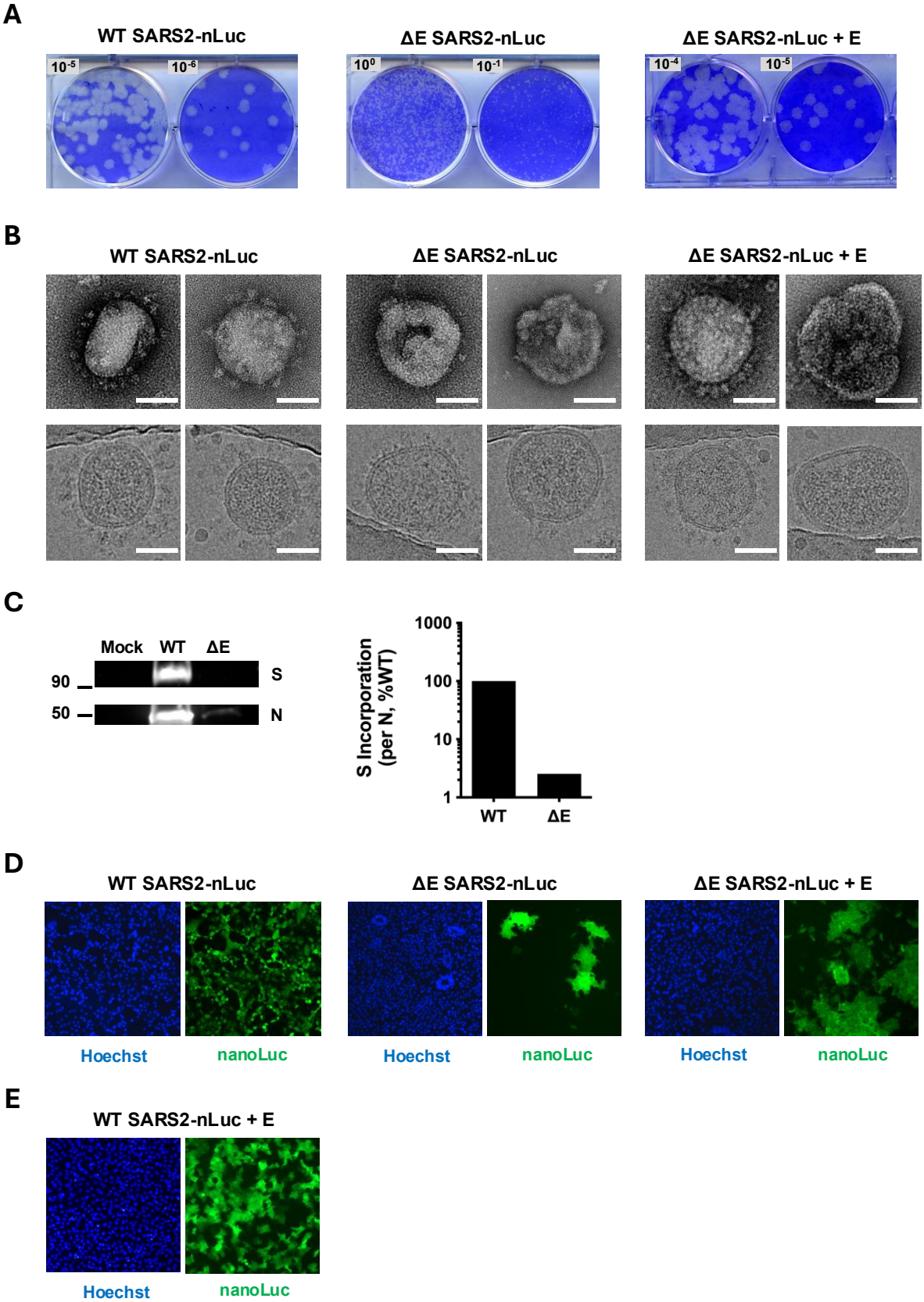
A
WT SARS2-nLuc
ΔE SARS2-nLuc
ΔE SARS2-nLuc + E
10-5
10-6
100
10-1
10-4
10-5
B
WT SARS2-nLuc
ΔE SARS2-nLuc
ΔE SARS2-nLuc + E
C
Mock
WT
ΔE
90
50
S
N
S Incorporation (per N, %WT)
1000
100
10
1
WT
ΔE
D
WT SARS2-nLuc
ΔE SARS2-nLuc
ΔE SARS2-nLuc + E
Hoechst
nanoLuc
Hoechst
nanoLuc
Hoechst
nanoLuc
E
WT SARS2-nLuc + E
Hoechst
nanoLuc

Figure 4

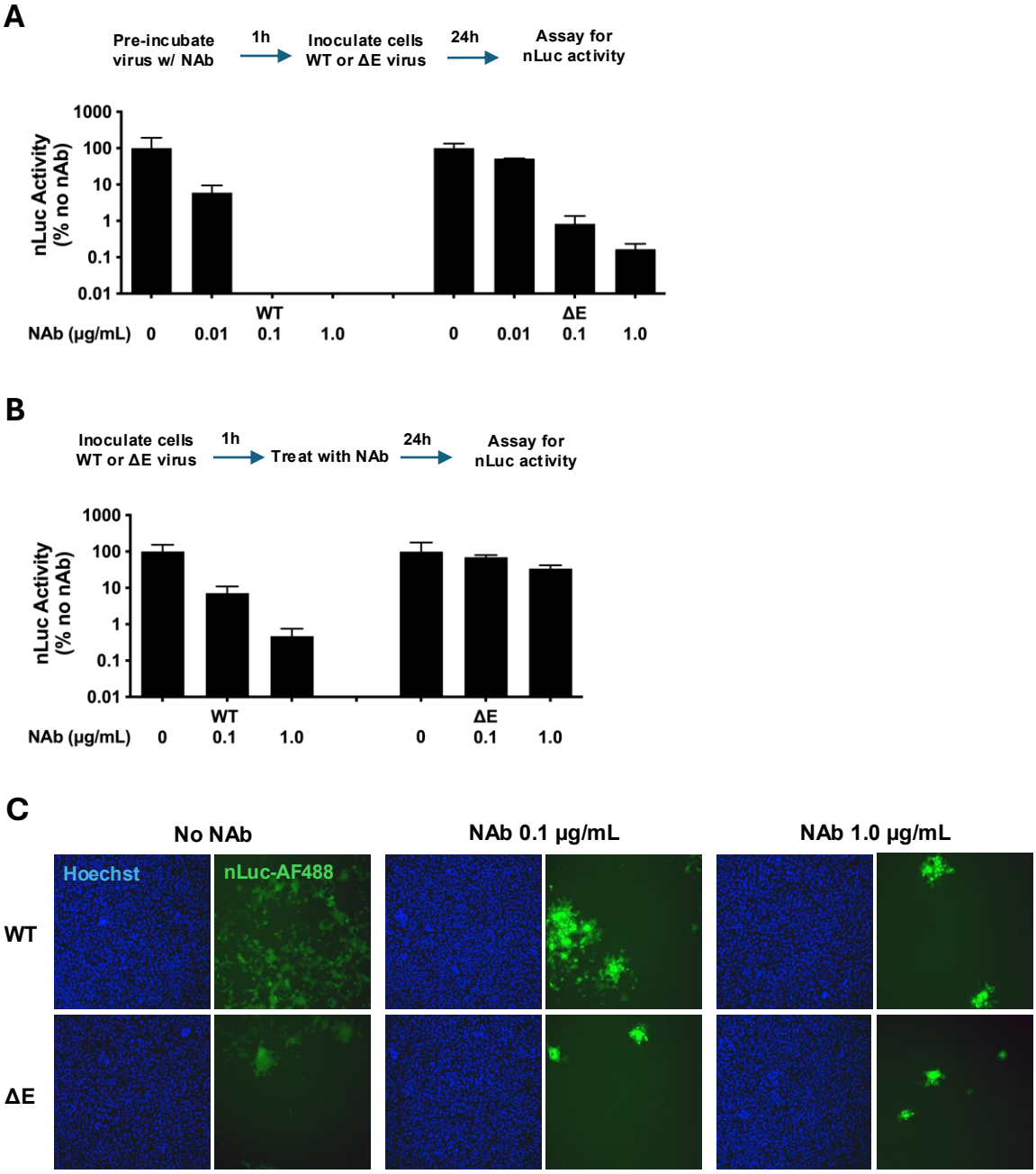
A
Pre-incubate virus w/ NAb
1h
Inoculate cells WT or ΔE virus
24h
Assay for nLuc activity
nLuc Activity (% no nAb)
1000
100
10
1
0.1
0.01
WT
ΔE
NAb (µg/mL) 0 0.01 0.1 1.0 0 0.01 0.1 1.0
B
Inoculate cells WT or ΔE virus
1h
Treat with NAb
24h
Assay for nLuc activity
nLuc Activity (% no nAb)
1000
100
10
1
0.1
0.01
WT
ΔE
NAb (µg/mL) 0 0.1 1.0 0 0.1 1.0
C
No NAb
NAb 0.1 µg/mL
NAb 1.0 µg/mL
Hoechst
nLuc-AF488
WT
ΔE

Figure 5

A

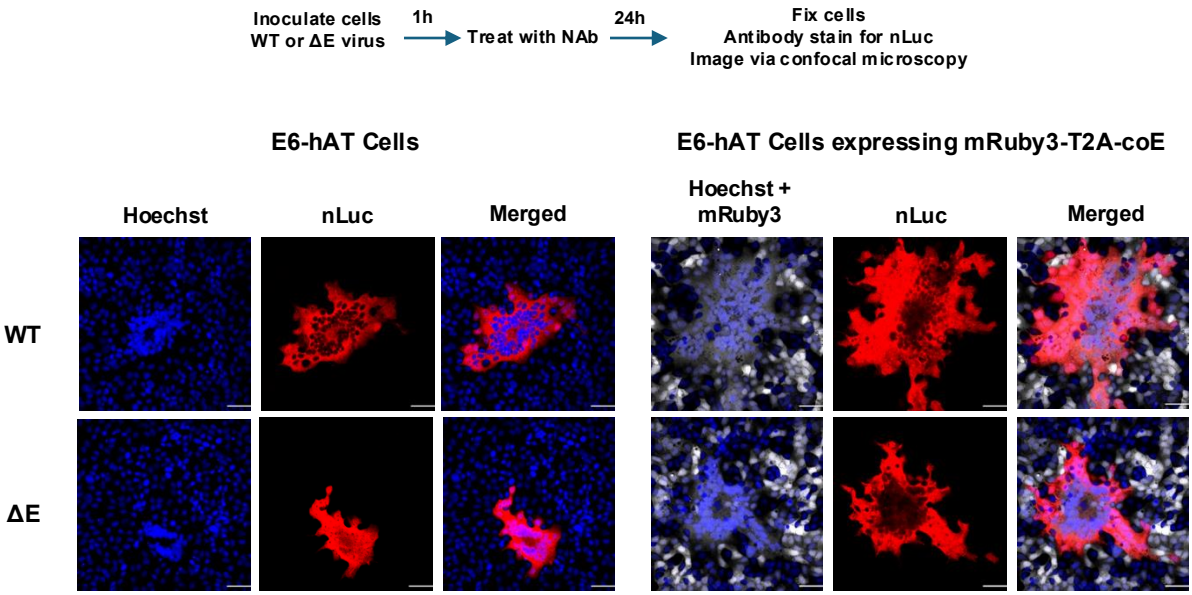
Inoculate cells
WT or ΔE virus
1h
Treat with NAb
24h
Fix cells
Antibody stain for nLuc
Image via confocal microscopy
E6-hAT Cells
E6-hAT Cells expressing mRuby3-T2A-coE
Hoechst
nLuc
Merged
Hoechst +
mRuby3
nLuc
Merged
WT
ΔE

B

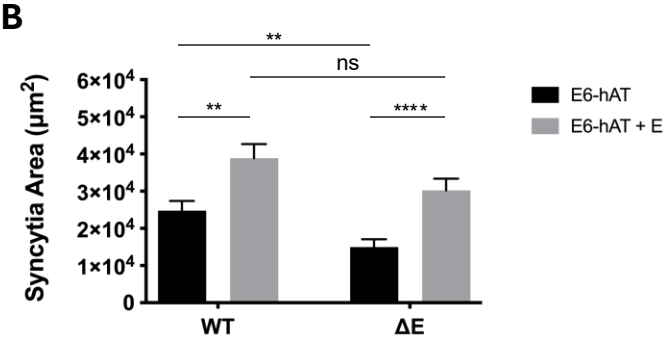
**
ns
**
****
Syncytia Area (μm²)
6×10⁴
5×10⁴
4×10⁴
3×10⁴
2×10⁴
1×10⁴
0
WT
ΔE
E6-hAT
E6-hAT + E

Figure 6

A

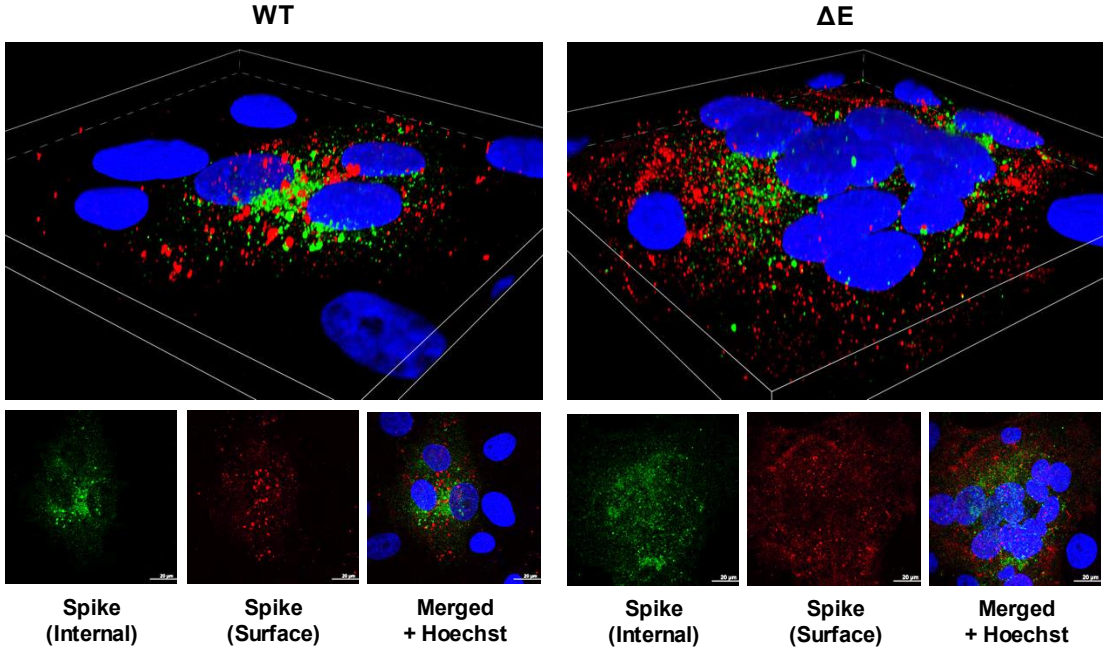
WT
ΔE
Spike
(Internal)
Spike
(Surface)
Merged
+ Hoechst
Spike
(Internal)
Spike
(Surface)
Merged
+ Hoechst

B

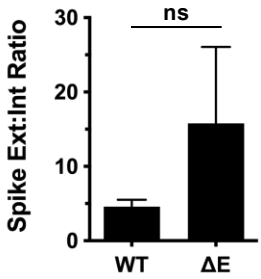
ns
Spike Ext:Int Ratio
30
20
10
0
WT
ΔE

Figure 7

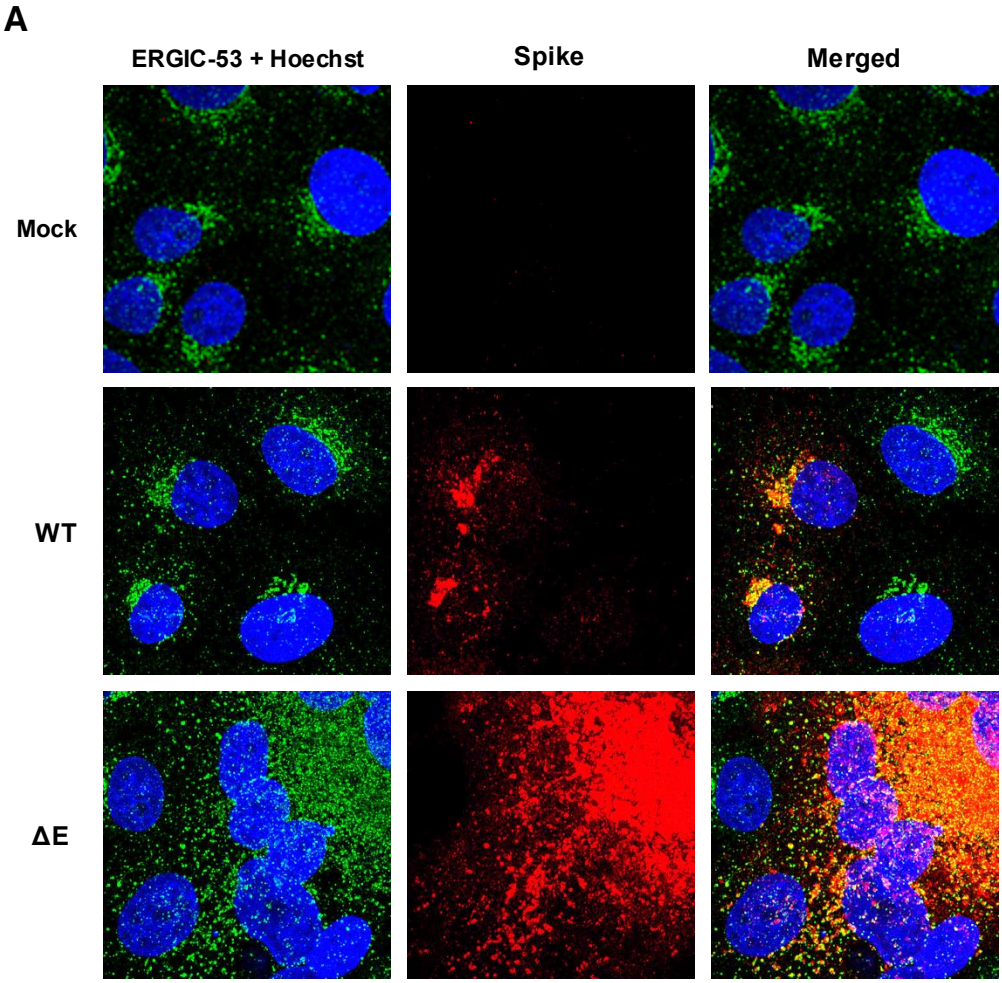
A
ERGIC-53 + Hoechst
Spike
Merged
Mock
WT
ΔE

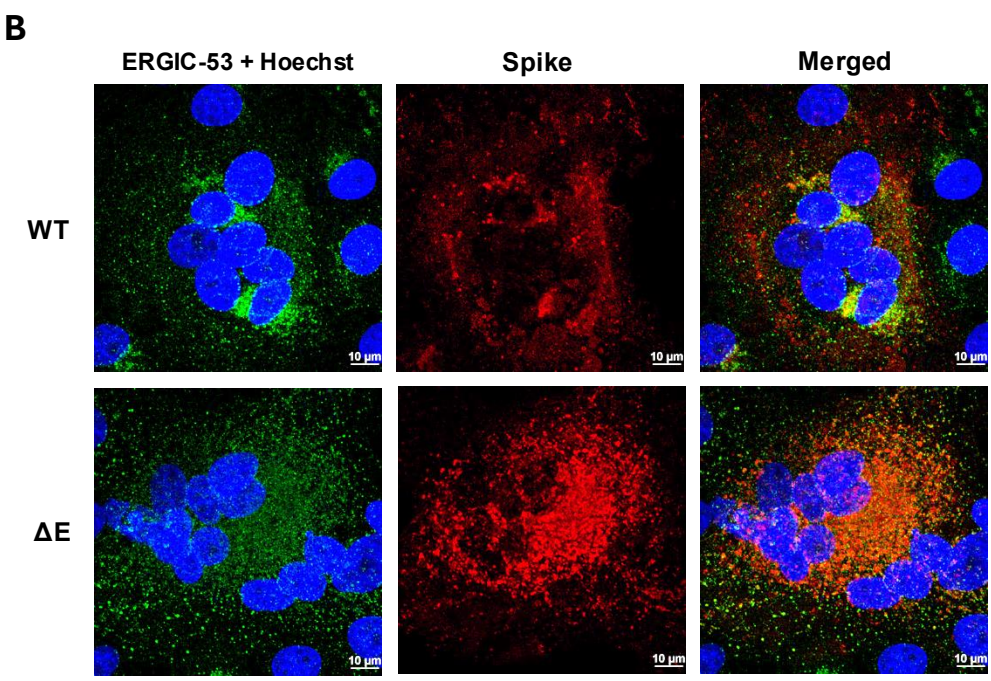
B
ERGIC-53 + Hoechst
Spike
Merged
WT
ΔE
10 µm

Figure 8

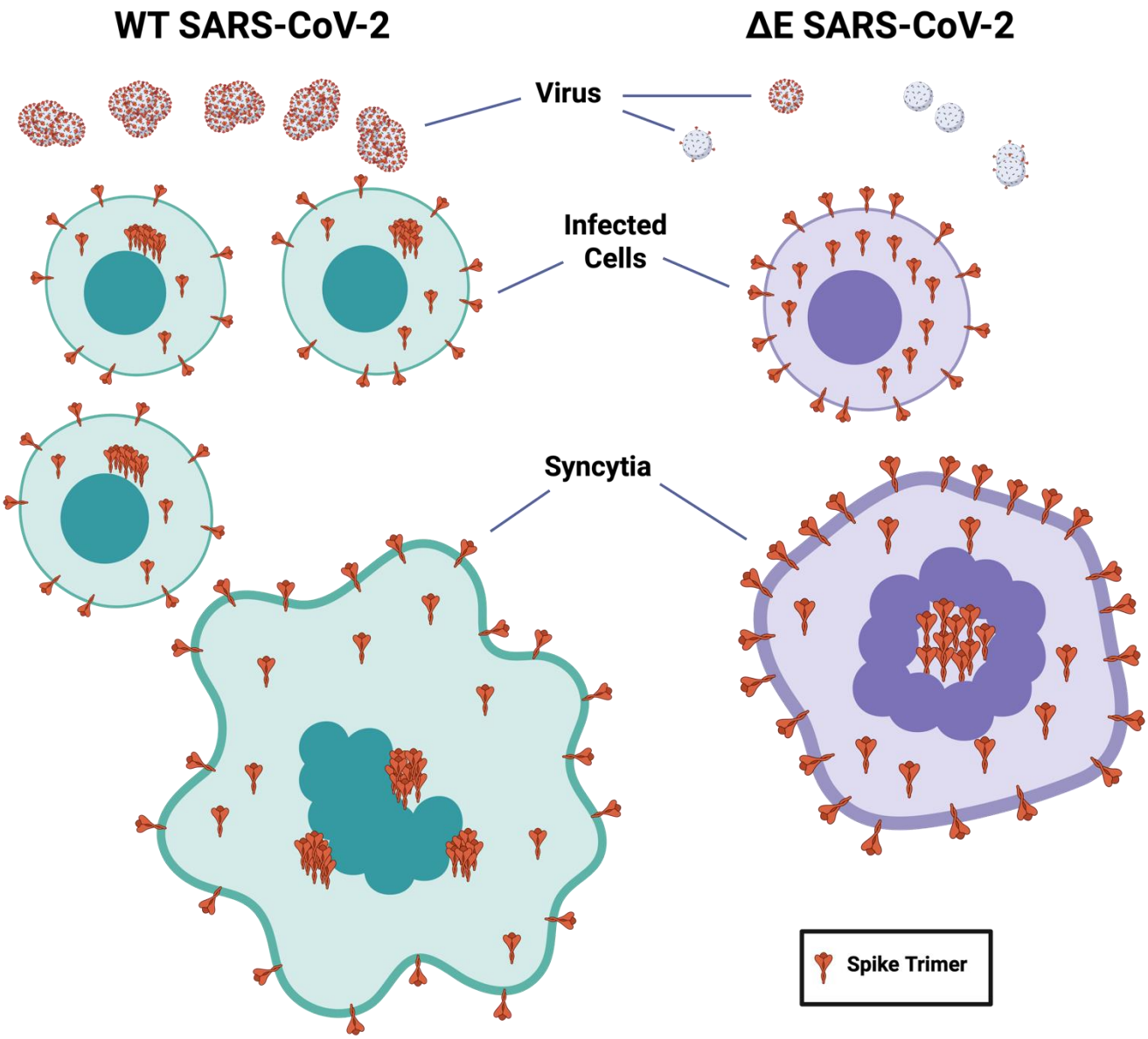
WT SARS-CoV-2
ΔE SARS-CoV-2
Virus
Infected Cells
Syncytia
Spike Trimer

Figure 9